REPORT DOCUMENTATION PAGE		*Form Approved* *OMB No. 0704-0188*

The public reporting burden for this collection of information is estimated to average 1 hour per response, including the time for reviewing instructions, searching existing data sources, gathering and maintaining the data needed, and completing and reviewing the collection of information. Send comments regarding this burden estimate or any other aspect of this collection of information, including suggestions for reducing the burden, to Department of Defense, Washington Headquarters Services, Directorate for Information Operations and Reports (0704-0188), 1215 Jefferson Davis Highway, Suite 1204, Arlington, VA 22202-4302. Respondents should be aware that notwithstanding any other provision of law, no person shall be subject to any penalty for failing to comply with a collection of information if it does not display a currently valid OMB control number.
PLEASE DO NOT RETURN YOUR FORM TO THE ABOVE ADDRESS.

1. REPORT DATE *(DD-MM-YYYY)*	2. REPORT TYPE	3. DATES COVERED *(From - To)*
07/09/2017	Final Performance Report	24 Sept. 2014 - 31 May 2017

4. TITLE AND SUBTITLE	5a. CONTRACT NUMBER
Flow Control of Flexible Structures	FA7000-14-2-0018
	5b. GRANT NUMBER
	5c. PROGRAM ELEMENT NUMBER

6. AUTHOR(S)	5d. PROJECT NUMBER
Farnsworth, John, A. N.	
Culler, Ethan, C.	5e. TASK NUMBER
	5f. WORK UNIT NUMBER

7. PERFORMING ORGANIZATION NAME(S) AND ADDRESS(ES)	8. PERFORMING ORGANIZATION REPORT NUMBER
Ann and H.J. Smead Department of Aerospace Engineering Sciences University of Colorado Boulder 429 UCB Boulder, CO 80309	

9. SPONSORING/MONITORING AGENCY NAME(S) AND ADDRESS(ES)	10. SPONSOR/MONITOR'S ACRONYM(S)
USAF Academy 8110 Industrial Dr. Ste 200 USAF Academy, CO 80840	
	11. SPONSOR/MONITOR'S REPORT NUMBER(S)

12. DISTRIBUTION/AVAILABILITY STATEMENT
Approved for public release, distribution is unlimited.

13. SUPPLEMENTARY NOTES

14. ABSTRACT
The kinematics and flow field development of two wing sections undergoing stall flutter limit cycle oscillations was thoroughly investigated with the goal of elucidating future pathways for successfully implementing aerodynamic flow control on flexible wing structures. A cyber-physical system was implemented with each wing section to prescribe and tune, in-situ, the torsional dynamics of the wing structure. The flexible wing kinematics were found to be accurately represented by the first three-eigenmodes of a beam in free vibration and the flow field was characterized by a small parabolic region of flow separation centered around 75% span and at the wing trailing edge.

15. SUBJECT TERMS
stall flutter, dynamic stall, cyber-physical system

16. SECURITY CLASSIFICATION OF:			17. LIMITATION OF ABSTRACT	18. NUMBER OF PAGES	19a. NAME OF RESPONSIBLE PERSON
a. REPORT	b. ABSTRACT	c. THIS PAGE			
					19b. TELEPHONE NUMBER *(Include area code)*

Standard Form 298 (Rev. 8/98)
Prescribed by ANSI Std. Z39.18

Flow Control for Flexible Structures

John Farnsworth

Ann and H.J. Smead
Department of Aerospace Engineering Sciences
University of Colorado Boulder
Boulder, CO 80309

Prepared for:

Aeronautics Research Center
United States Air Force Academy (USAFA)
Colorado Springs, CO
Attn: Thomas E. McLaughlin

September 6, 2017

Ann and H.J. Smead
Department of Aerospace Engineering Sciences
UNIVERSITY OF COLORADO **BOULDER**

Table of Contents

Abstract

The kinematics and flow field development of two wing sections undergoing stall flutter limit cycle oscillations was thoroughly investigated with the goal of elucidating future pathways for successfully implementing aerodynamic flow control on flexible wing structures. A cyber-physical system was implemented with each wing section to prescribe and tune, in-situ, the torsional dynamics of the wing structure. The first wing section studied was a flexible, semi-span, rectangular wing section composed of a NACA 0018 profile and having a semi-span aspect ratio of six. When tuned appropriately, the wing was able to maintain repeatable stall flutter limit cycle oscillations, which were dominated by primarily torsional motions. The torsional and bending kinematics were found to be accurately represented the first three eigenmodes of a fixed-free beam in free vibration. When analyzing the flowfield it was found that a coherent dynamic stall vortex was not produced in contrast to prior work on rigid wings. Instead the wing stall and flow separation was dominated by the growth and collapse of a small parabolic region of flow separation centered around 75% span location and at the wing trailing edge. The second wing section studied was a rigid, full-span, rectangular wing section composed of a NACA 0018 profile and having an aspect ration of 4. Instead of undergoing a twisting deformation this wing was constrained to a rigid-body pitching motion in the wind tunnel and was used to identify the differences between prescribed sinusoidal pitching motion and passively sustained stall flutter. Specifically, it was found that stall flutter displays a slower pitch-up rate as compared to classically prescribed sinusoidal motions. This slower pitch-up rate reduced the maximum magnitude of the induced pitching moment and the coherence of the primary dynamic stall vortex that was formed.

List of Figures

List of Tables

Acknowledgments

1 Summary

The following final performance report documents the technical research conducted by the principle investigator (PI) and his graduate research assistant (GRA), Ethan Culler, during the full performance period (September 24, 2014 through May 31, 2017) of cooperative agreement number FA7000-14-2-0018 entitled *Flow Control of Flexible Structures*. This report focuses on the technical progress and achievements under this agreement, with the financial progress reported separately in quarterly financial reports as documented in the cooperative agreement.

The final report is structured to address the technical objectives that were laid out in the original proposal. As a result the original scientific objectives are summarized here in Section 2.1 which is followed by a brief discussion of deviations from the proposed effort in Section 2.2. It should be noted that an extensive literature review is not included in this report for brevity; if readers are interested in a more detailed discussion of the prior work they are referred to journal and conference publications that were published as a result of this effort which are listed in Section 7. Instead this report will focus on the scientific results and accomplishments made under this research effort. As a result the experimental methodology is discussed in detail in Section 3 which is followed by a thorough discussion of the experimental results and findings in Section 4. Additionally, the results section is divided into to subsections which align with the two major phases of the proposed effort. The first phase, (Section 4.1) focused on the detailed analysis of the wing kinematics and flowfield development for the flexible cyber-physical wing system undergoing stall flutter. These experiments were carried out in the Subsonic Wind Tunnel at the United States Air Force Academy (USAFA) and the results were then analyzed by the PI and GRA back at the University of Colorado Boulder (UCB). The second phase of the research effort (Section 4.2) focused on elucidating the differences between a rigid wing undergoing sinusoidal prescribed motion and passivily sustained stall flutter limit cycle oscillations (LCOs). These experiments were carried out at both the USAFA and UCB and again the results were analyzed by the PI and GRA at UCB. The detailed discussion of the results, is followed by a brief summary of the accomplishments of this research effort (i.e. publications, presentations, and awards) in Section 7. The a summary of the scientific conclusions from the research effort is made in Section 5, which is followed by a brief discussion of recomendations for future work in Section 6.

2 Introduction

Fluid-structure interactions have long been a research topic of great interest. However, to date, most investigations regard the fluid dynamics problem as too complex to be fully understood and therefore resort to various levels of modeling [Dowell and Hall, 2001]. Furthermore, even for the most complex models, the main research goal has been a mathematical description of the structural dynamics with the flow merely providing the "forcing term" [Barone and Payne, 2005]. With recent advances in computational and experimental technology, however, it is now possible to consider what can be learned about the unsteady physical processes in the flowfield that eventually result in structural deformations. Ultimately, research in fluid-structure interaction can show ways to tailor the flowfield (using feedback flow control) or the structure (using adaptive materials and active structural con-

trol) to accomplish a prescribed objective.

A comparison of the dynamic behavior of fluid flowing over a flexible structure and the structure itself reveals that there are fundamentally different time scales in the fluid and structural dynamics, where the fluid dynamic processes occur on a significantly faster time scale and a concomitantly shorter length scale. In fact, recent research unequivocally shows that the response of a structure to aerodynamic loading has to be understood as the integral effect of the faster and smaller scale fluid dynamics occurring in the flow around the structure [Mangalam et al., 2008]. Therefore, sensing and controlling the fluid dynamics instead of solely measuring and controlling the structural deformation (e.g. with accelerometers) provides two key advantages: i) early detection of flowfield changes that will eventually result in structural loads, and ii) the possibility for localized, discrete actuation to counteract detrimental flow developments before they result in significant structural loads and deformations. If such sensing and control is possible, significant improvements to engineering systems can be expected. Applications such as renewable energy systems (e.g. wind turbines or ocean energy devices), air vehicle aerodynamics and engines, or even medical flows (blood flow, respiration) could be better understood and therefore their performance could be improved.

Aerodynamically, fluid-structure interactions can be primarily placed in two categories: those that are induced by lift and those induced by drag. For lift-induced fluid-structure interaction, controlling the lift distribution provides a means to control the structural deformation. This is the classical aeroelasticity problem, for which passive and active structural control strategies have been thoroughly investigated [Fung, 1955, Librescu and Marzocca, 2005]. As a result this represents the primary focus of the current research.

From an active flow control perspective, nature provides insight into how aeroelastic systems can be controlled: with sophisticated methods integrating instantaneous distributed flow state sensing and control actuation. Birds, for example, use their feathers as both sensors to monitor the local flow state and as actuators to achieve local flow control. Bats, on the other hand, use fine hairs sparsely distributed on their wings to sense the air flow and morph their wings through altering the wing geometry and the tension in the wing membrane, as necessary to achieve a desired flight path in the instantaneous prevailing flow conditions [Sterbing-D'Angelo et al., 2011]. Clearly, nature has developed tightly coupled control systems, employing flow control and structural control simultaneously. To mimic these tightly coupled feedback control systems, sensors, actuators, and control strategies need to be developed to achieve control of flexible structures while maintaining aerodynamic system performance. A thorough understanding of the underlying flowfield, including the effects of structural flexibility, is crucially important for the eventual development of feedback flow control on flexible structures in technical applications.

2.1 Proposed Research Effort

A collaborative research program was originally proposed with the goal of achieving active flow control on flexible structures through a progressive sequence of research objectives. That said the proposed effort focused on understanding the fundamental fluid dynamics associated with the fluid-structure interaction problem with the goal of determining how the implementation of open-loop fluidic actuation directly alters the fluid dynamics and indirectly alters the structural dynamics. To achieve this goal the original proposal laid out

the following scientific objectives:

1. To determine if the same three-dimensional unsteady vortical structures are formed and shed from a passively driven (driven solely by the oncoming flow) aeroelastic wing as compared to an actively oscillated wing model at a moderate Reynolds number.

2. To investigate the role of the flow velocity and material stiffness in the formation and growth of the unsteady structures in the flowfield and thus the structural oscillations.

3. To determine from the passive (unforced) characteristics the optimal locations for actuation and sensing devices on the flexible wing surface.

4. To investigate whether fluidic actuators can be utilized to both amplify and cancel the formation and growth of the unsteady vortical structures.

5. To determine if the different vortex wake modes (and thus aerodynamic loads) can be generated through exciting the flowfield and structure with small local alterations to the unsteady flowfield, without changing the free-stream velocity, material properties, or mechanically driving the wing.

2.2   Deviations from Proposed Effort

As highlighted above, the proposed research represented a collaborative effort which was closely coordinated with research efforts in the Aeronautics Laboratory at USAFA lead by Dr. Jürgen Seidel and Dr. Casey Fagley. The progress of the collaborative research effort was regularly reviewed throughout the performance period by the group (i.e. Dr. Seidel, Dr. Fagley, the GRA and PI). The short term plans for the future research were then made by the group based upon the achieved progress and resources available at each of the sites (i.e. USAFA and UCB). This coordination and planning allowed the research effort to stay on task, but also allowed for deviations for the proposed effort to be coordinated as needed.

The most significant deviation from the proposed effort was related to the implementation of flow control on the flexible wing system. In the original proposal a significant amount of effort was focused on implementing flow control in the flexible wing. This included objectives 3, 4, and 5 in Section 2.1. It was realized early on by the group that accomplishing all of these tasks was overly ambitious with the limited availability of the Subsonic Wind Tunnel (at USAFA) during the summer testing periods. As a result the, GRA and PI focused primarily on the detailed investigations into the baseline kinematics and flowfield surrounding the flexible wing in stall flutter during the first summer testing period (May - August 2015). During the second summer testing period (May - August 2016), the Subsonic Wind Tunnel at USAFA was being upgraded which significantly limited the available testing time for the proposed research. As a result the GRA and PI worked during the second summer period to construct a second cyber-physical testing assembly at UCB. Once operational, this allowed tests to be carried out at UCB in the low-speed research wind tunnel, which had less limitations on availability. Specifically, the testing at UCB focused on quantifying the differences in the kinematics and flowfield development between a rigid wing body in passively sustained stall flutter limit cycle oscillations and the same wing actively pitched (or driven) in similar periodic oscillations. Results and analysis of both the flexible wing and the rigid wing problems will be presented in detail below below in Section 4 after a thorough discussion of the experimental facilities and measurement techniques in Section 3.

3 Methodology

The research carried out as a part of this effort focused entirely on experimental measurements of two distinctly different fluttering wing models, namely: 1) a semi-span, flexible wing model undergoing spanwise varying twisting oscillations and 2) a full-span, rigid wing model undergoing spanwise uniform pitching oscillations. Note that a cyber-physical approach was utilized to dynamically prescribe the motions for both of these model configurations. Finally, as part of the research program measurements were collected in both the subsonic wind tunnel at USAFA and the low-speed research wind tunnel at UCB. The following subsections provide additional details about both of these facilities, each of the model configurations, and the measurement techniques utilized.

3.1 Subsonic Wind Tunnel, USAFA

The United States Air Force Academy's Subsonic Wind Tunnel is located in the Aeronautics Research Center and was fabricated by FluiDyne Engineering. It is a single leg recirculating type wind tunnel and has a $0.91\ m$ by $0.91\ m$ by $1.83\ m$ test section. It is capable of attaining speeds up to Mach numbers of $M = 0.5$, however for most of the tests discussed here the wind speed was limited to $U_\infty = 26\ m/s$ or $M = 0.08$. The tunnel facility is instrumented with a MKS Baratron 220C transducer to measure the dynamic pressure in the test section.

3.2 Low-Speed Research Wind Tunnel, UCB

The Low-Speed Research Wind Tunnel in the Experimental Aerodynamics Laboratory at the University of Colorado Boulder was designed and fabricated by Aerolab LLC. It is a open-return facility with an upstream centrifugal blower and has a test section of 0.76 m by 0.76 m by 3.5 m in length. It is capable of attaining speeds up to Mach numbers of $M = 0.2$, however again for most of the tests discussed here the wind speed was limited to $U_\infty = 15\ m/s$ or $M = 0.04$. The tunnel facility is instrumented with a MKS Baratron 220D transducer to measure the dynamic pressure, a MKS Baratron 220A to measure the static pressure, and a T-Type thermocouple to measure the total temperature within the test section.

3.3 Cyber-Physical System

The stall flutter limit cycle oscillations of the two wing models were tuned using the position-feedback cyber-physical control system originally developed by Fagley et al. [2015, 2016] and pictured in Figure 1 for the flexible wing model. The rigid wing cyber-physical system assembly was very similar and is pictured in a horizontal orientation in Figure 6. For the flexible wing experiments conducted at USAFA, the actual cyber-physical system developed and employed by Fagley et al. [2015, 2016] was utilized. As part of the current research effort, a replica of this cyber-physical system was built at UCB and utilized for the rigid wing experiments. In both cases, an embedded controller was designed to take the form of a second-order mass-spring-damper system as shown in Equation (1). The angle of attack was determined from a $16,000$ count optical encoder, while the angular velocity and angular acceleration were calculated with the embedded FPGA on a National Instruments CRIO-9063. This produced an angle of attack measurement precision of 0.02^o with an FPGA
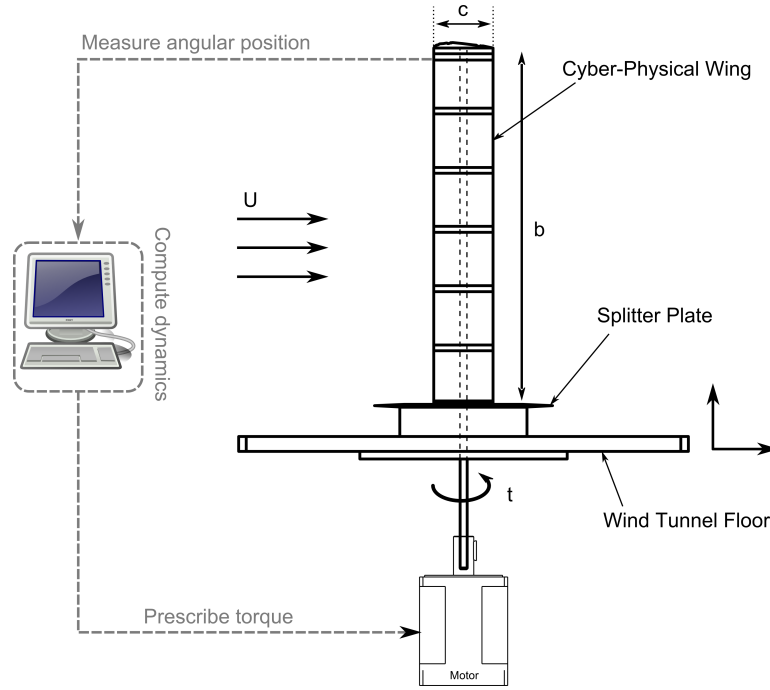
Figure 1: Illustration of the cyber-physical system which uses feedback control to simulate the torsional structural dynamics of the flexible wing model. [Fagley et al., 2015].

output update every 2 ms.

$$J_V \ddot{\theta} + \eta_V \dot{\theta} + k_\theta \theta = \tau_{Motor}. \tag{1}$$

Using this cyber-physical system approach, the rotational stiffness, k_θ, virtual rotational damping η_V, and virtual rotational inertia, J_V, were tuned through a respective change in the control system gains. In Equation (1), θ is the tip-twist angle (flexible wing) or rigid-body rotation angle (rigid wing) with respect to its unforced or wind off position and τ_{Motor} is the applied torque. Furthermore, the reference position for θ is the geometric angle of attack, α_o. Thus the model's structural dynamics could be easily adjusted in-situ without requiring physical modifications to the wing model. The second order dynamical system is prescribed as shown by the control system block diagram in Figure 2.

3.4   Flexible Wing Model

The test geometry for the flexible wing model consisted of a finite span NACA 0018 wing model cantilevered up from a splitter plate mounted to the wind tunnel floor as shown in Figure 1. Note that the splitter plate was utilized to isolate the influence of the tunnel boundary layer from the wing model aerodynamics. The wing had a chord and span of $c = 0.1$ m and $b = 0.6$ m, respectively, producing a semi-span aspect ratio of $AR = 6$.

To ensure that the structural dynamics are dominated by the virtually prescribed torsional properties, the wing segments were constructed from molded urethane rubber sections with plastic ribs printed using a stereolithography (SLA) technique. The model was built in five interlocking sections allowing for quick modification of stiffness parameters and the
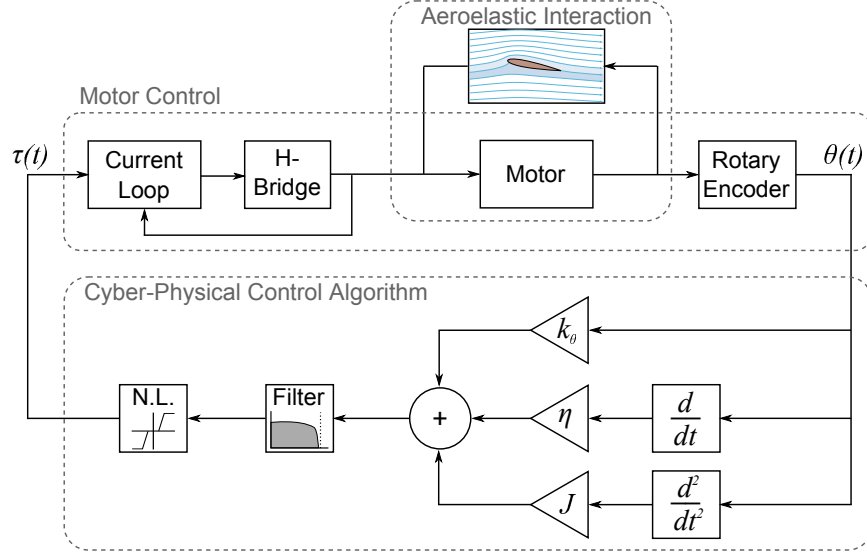
Figure 2: Block diagram of the cyber-physical control system. [Fagley et al., 2015].

incorporation of different sensing transducers at various points along the span. In this configuration the model leading edge was stiffened by a 6.4 mm carbon fiber spar to ensure a quasi-linear structure at the tested wind speeds, as validated by the results in Section 4. Furthermore, the cyber-physical system was used to prescribe a torsional stiffness, torsional damping and torsional inertia of $k_\theta = 0.47\ N\ m\ rad^{-1}$, $\eta_P = 6.09 \times 10^{-3}\ N\ m\ s\ rad^{-1}$, and $J_P = 4.25 \times 10^{-4}\ kg\ m^2\ rad^{-1}$, respectively. These structural properties were confirmed through system identification of the model's response to a step input as described in Fagley et al. [2015, 2016]. Finally it should be noted that the stall flutter onset velocity for a nearly identical model was experimentally tested and shown to occur at approximately 20 m/s in Fagley et al. [2016], placing the current experiments within the post-flutter regime.

3.5   Rigid Wing Model

The test geometry for the rigid wing model consisted of a finite span, NACA 0018 cross-section, rectangular wing model with a chord and span of $c = 0.15$ m and $b = 0.6$ m, respectively. This produced a wing aspect ratio, $AR = 4$. Note that the wing model was centered on a rotational shaft which symmetrically spanned to the wind tunnel floor and ceiling producing a symmetric finite span wing with two "effectively" free tips. Additionally, the rotation axis was located at 50% chord (i.e. $x/c = 0.5$). Finally, the rigid wing was constructed from three interlocking plastic sections printed using a stereolithography technique.

For the rigid wing experiments, the cyber-physical system dynamics were varied over a range of virtually prescribed stiffness and damping values while the virtual inertia, J_V, was left fixed at zero. The physical interita J_P and physical mechanical damping η_P of the wing model system were estimated through system identification of the model's response to a step input as described in Fagley et al. [2015, 2016]. This resulted in a value of $J_P \approx 3(10^{-3})$ kg m^2/rad and $\eta_P \approx 1.2(10^{-2})$ Nm s/rad.

The rigid wing was also tested undergoing a prescribed (or driven) sinusoidal motion for

comparison with the stall-flutter results produced through the cyber-physical control system. This was accomplished by switching the mechatronic system from the cyber-physical mode into a standard position control mode. The position control was accomplished using a Copely Controls Accelnet Micro Panel ACJ-090-12 motor controller with a 0.3 ms update rate using a combination of PID control with feed-forward velocity and acceleration gains to further reduce following errors. Using this approach the periodic, angular trajectory of the wing was then defined by a single frequency sine wave as given by Equation (2).

$$\alpha(t) = \overline{\alpha} + A sin(\omega t) \tag{2}$$

Note that the offset $\overline{\alpha}$, the pitch amplitude, A and pitch angular frequency, ω, were defined based upon empirical trajectories of the stall flutter limit cycle oscillations measured in the cyber-physical mode of operation.

3.6   Stereoscopic Motion Capture System

The stereo vision data was captured using two synchronized high-speed Phantom cameras from Vision Research (models V711 and V7.3). The cameras were positioned in a stereoscopic configuration parallel to the wind tunnel floor, approximately 1.7 m laterally away from the wind tunnel center-line with a 32° angular separation, as depicted in Figure 3. To provide the best contrast for the motion capture program the wing was painted black and white adhesive dots were affixed to the surface. The dots had a diameter of 9 mm and were positioned on the wing in a rectangular grid with chord-wise positions of $x/c = 0.1$, 0.3, 0.5, 0.7, and 0.9 and spanwise positions of $z/b = 0.38$, 0.58, 0.78, and 0.98, as detailed in Figure 4. It should be noted that these spanwise dot locations were selected to align with the rigid SLA ribs in the model. The stereo vision data was captured at a sampling frequency of $f_s = 1\ kHz$ for a period of $\Delta t = 20\ s$ during the wing stall flutter motion.

The image sequences were then processed using a direct linear transformation (DLT) technique in the Matlab programming environment with the Digitizing Tools version 5 toolbox from Hedrick [2008]. The raw coordinate data produced by the stereo-vision system was oriented in the standard wind-tunnel aligned Cartesian system (x, y, z) as presented in Figure 5. Note that, the stereo vision measurements were only made on the flexible wing model, as a result their discussion focuses upon the local twist displacement, θ, which is defined as the difference between the instantaneous, local angle of attack and the root angle of attack of the flexible wing model. The translational displacement of the wing coordinates in the cross-stream, y, direction will also be presented as T_y. The chordwise and spanwise translational displacements of the wing model, T_x and T_z respectively, will not be presented as they were found to be negligible and within the experimental uncertainty. The uncertainties in the cross-stream bending and twist displacements were estimated to be $\delta(T_y) = \pm 0.85\ mm$ and $\delta(\theta) = \pm 1.6^o$, respectively. Note that these were determined from a combination of the calibration error and the error associated camera pixel resolution. Furthermore, the uncertainty is computed from the spatial average of the uncertainties across the entire calibration range in the x and y directions.

The stereo-vision data was also utilized to validate the tip-twist measurements made internally within the cyber-physical system. As such the stereo-vision image capture was also precisely synchronized to the measurement of the wing-tip angular position from the motor shaft optical encoder which has a resolution of 16,000 counts per revolution or 0.02^o
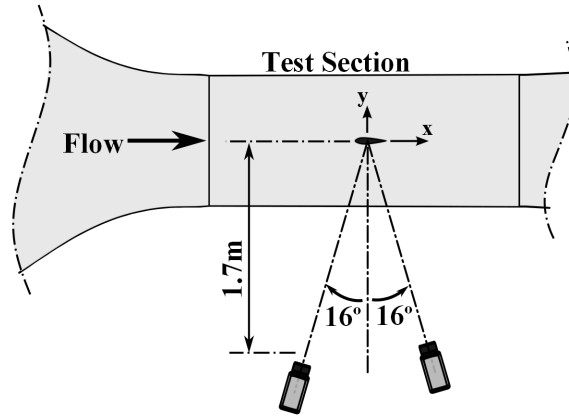
Figure 3: Schematic defining the stereo-vision camera orientation with respect to the wing mounted in wind tunnel (Top View).
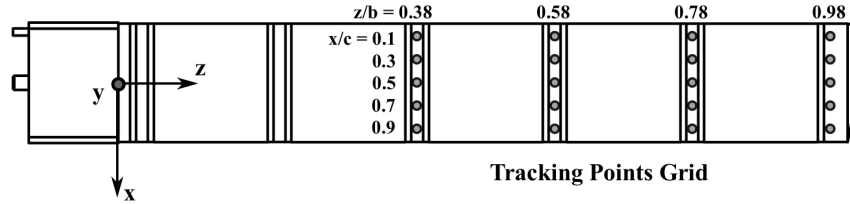
Figure 4: Schematic detailing the stereo vision tracking point layout along wing span and the coordinate system orientation.

per count. For more detail about the cyber-physical system configuration see Fagley et al. [2015, 2016].

3.7   Planar and Stereoscopic Particle Image Velocimetry

Both planar particle image velocimetry data (PIV) and stereoscopic particle image velocimetry (SPIV) data was collected using the same LaVision sysem. The system utilized upto two Imager SCMOS cameras with 2560 x 2160 resolution and 16 bit intensity. The cameras were fitted with either a Nikkor $f = 60\ mm$ or a Nikkor $f = 105\ mm$ fixed focal length macro lens producing scale factors of 10.2 pixels/mm and 19.8 pixels/mm, respectively. Note that the $f = 60\ mm$ lens was used in the planar PIV studies while the $f = 105\ mm$ lenses were used for SPIV. The flowfield was seeded using a ViCount Compact 1300 smoke machine which generated $\mathcal{O}(1\ \mu m)$ particles in physical size or $2 - 3$ pixels in the scaled images. The planar fields were illuminated by a laser sheet which was produced by a Quantel Evergreen 200 532 nm dual pulsed Nd-YAG laser which had a 200 mJ maximum output energy. For both planar and stereo measurements, the laser was configured with a $f = -10\ mm$ cylindrical lens oriented to produce a laser sheet that illuminated a single chord-wise section of the wing span. The cameras and laser head were mounted on separate Velmex two axis traverses allowing for accurate positioning of the PIV system. The traverses had an
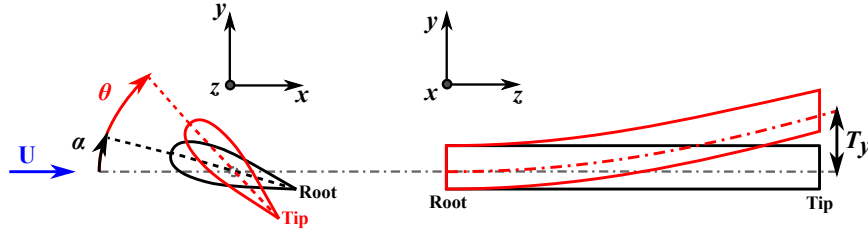
Figure 5: Schematic defining the bending and twisting deflections in the wing and wind tunnel coordinate systems.

accuracy of $\pm$ 0.006 mm and were utilized to scan the wing Due to the periodic nature of the achieved stall flutter oscillation, the PIV data was taken phase locked to the angular position of wing or flexible wing tip, as recorded by the cyber-physical system encoder. Note that the $16,000$ct encoder had a resolution of 0.02^o.

For the SPIV study on the flexible wing measurements were taken at multiple spanwise locations, namely: $z/b = 0.58$, 0.625, 0.71, 0.75, 0.79, and 0.875. At each spanwise location, three phase planes were taken at $\phi = 204^o$, 214°, and 224° to capture the progression of flow separation. Additionally for the spanwise location of $z/b = 0.75$, which approximately corresponded to the location of maximum separation, higher resolution phase data was collected at $\Delta\phi \approx 2^o$ between $\phi = 194^o$ and $\phi = 233^o$ and for two additional phase points at $\phi = 185^o$, and 243°. For each combination of spanwise and phase location, 500 image sets were collected with a $\Delta t = 20$ μs. These image sets were processed using LaVision's DaVis 8.3 program on the graphical processing unit (GPU). A multi-pass scheme was utilized where the initial pass utilized a guassian weighted 64 x 64 pixel interrogation window and two subsequent passes utilized 32 x 32 pixel windows, with an overlap of 75%. The raw images were individually masked along the surface reflection line resulting from the incident laser light on the wing.

Planar particle image velocimetry (PIV) data was also captured on the rigid wing model using the same LaVision system. In this case a single spanwise location at $z/b = 0.5$ was capture. Sets of 25 image-pairs were taken at 64 phase positions across the full cycle for the two operating modes. This resulted in time steps of 5 ms or phase steps of $\Delta\phi = 6^o$. The planar PIV data was processed using LaVision DaVis 8.3 software again on the GPU using a multi-pass method with an initial pass at 64 x64 pixels and two final passes at 32 x 32 pixels with a 50% overlap in the interrogation windows.

3.8 Pitching Moment Measurements

To understand the pitching moment results, a discussion of forces observed in the cyber-physical system is required. The resulting moment response was captured using a Futek TSS400 single-axis torque sensor installed inline between the cyber-physical system motor and the wing on the axis of rotation. This allowed the cyber-physical system to measure the net system pitching moment, $\tau_{Meas.}$, at the root of the wing. This measured pitching moment (torque) represents the summation of the aerodynamically imposed moment and resistive moment imposed by the physical inertia and damping of the wing. Additionally, this measured moment (torque) is equal to the torque produced by the motor. This balance is graphically shown in Figure 6 where η_P refers to physical damping imposed by the three
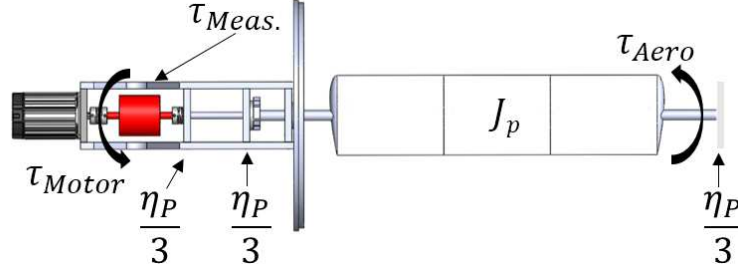
Figure 6: The balance of forces in the rigid-wing cyber-physical system.

bearings installed on the drive shaft.

Mathematically the force balance is given in Equation (3):

$$\tau_{Motor} = \tau_{Meas.} = \tau_{Aero.} - \tau_{Struct.} \tag{3}$$

where

$$\tau_{Struct.} = J_P\ddot{\theta} + \eta_P\dot{\theta}. \tag{4}$$

The aerodynamic pitching moment, $\tau_{Aero.}$ here represents the resultant of all circulatory and non-circulatory force contributions. This moment can be re-written as a pitching moment coefficient:

$$C_m \;=\; \frac{\tau_{Aero.}}{qSc}, \tag{5}$$

which is comparable to a traditional static moment coefficient measure. In dynamic pitching situations, added mass appears as a non-circulatory force and depending on the ratio of fluid density to structural inertia, this force can be quite significant. In this case, where the wing operates in air, the effect of this term can be approximated by assuming the wing accelerates a cylinder of air with radius $c/2$ and length b. The moment of inertia for this cylinder is given by $1/2Mr^2$. Using this approximation the inertial resistance due to added mass is given by $\rho\pi bc^4/32$ or $3(10^{-5})$ kg m^2. The wing system has an inertia of $\approx 3(10^{-3})$ kg m^2 indicating that the added mass is two orders of magnitude smaller and therefore negligible.

The measured moment τ_{Meas} provides a net system torque and is of interest as it represents the torque at the wing root. This would be the load transferred to the aircraft body, or in an energy harvesting configuration, the net energy extracted from the aeroelastic system. This paper will discuss both torques in terms of moment coefficients, utilizing the following two conventions: 1) Cm refers to the moment coefficient around the 50% chord location resulting from the aerodynamic pitching moment contribution $\tau_{Aero.}$ and 2) $Cm_{Meas.}$ refers to the moment coefficient of the measured or net system torque $\tau_{Meas.}$. As a note, the measured pitching moment $\tau_{Meas.}$ is filtered using a low-pass butterworth filter with 17.5 Hz cutoff frequency.

4   Results and Discussion

The results and discussion is divided into two primary sections below. First, the detailed investigation into the baseline kinematics and flowfield development surrounding the flexible wing model in stall flutter is presented in Section 4.1. Then, the response comparison (i.e.
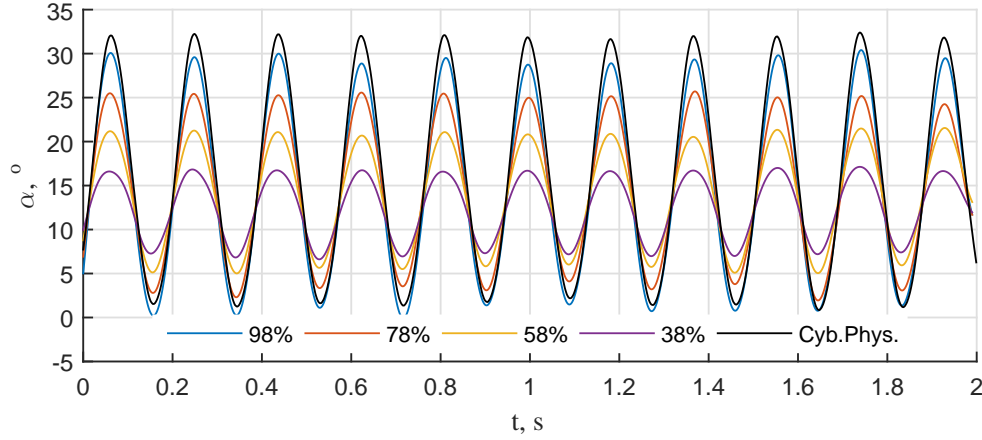
Figure 7: Time-history of the local angle of attack, α, obtained by the cyber-physical tip-twist encoder (black) compared against the stereo-vision motion tracking system measurements at spanwise positions of $z/b = 0.38$, 0.58, 0.78, and 0.98 (magenta, yellow, red, and blue respectively).

kinematic and flowfield) is made in Section 4.2 for the rigid wing model undergoing both passive stall-flutter limit cycle oscillations and prescribed pitch oscillations.

4.1 Flexible Wing Model

The resulting structural kinematics of the high-aspect-ratio, finite-span, flexible, cyber-physical wing system undergoing stall flutter are thoroughly presented in five subsections sections below. First in Section 4.1.1, a comparison is made between the cyber-physical system's encoder tip-twist angle measurement and the twist measurements made via the stereo-vision system; to cross-validate both measurement systems. Second in Section 4.1.2, a detailed discussion is presented of the trajectory, periodicity, and uniformity of the stall flutter limit cycle oscillations. Third, a fourier analysis of the time history is conducted in Section 4.1.3 which then leads to the eigenfunction projection in Section 4.1.4. The time-signals for each of the principal motions, torsion and bending, are decomposed into the modes given by the eigenfunction solutions from classical beam vibration theory. From this projection and fourier analysis, a kinematic relation for the wing motion is written in Section 4.1.5. Finally, following the discussion of the wing kinematics, the aerodynamics of the flexible wing system are thoroughly discussed. This begins with the analysis of the internal moments (torques), measured from the cyber-physical system, in Section 4.1.6. Then the flowfield surrounding the flexible wing is analyzed and discussed in Sections 4.1.7, 4.1.8, and 4.1.9 where the both the periodic and spatial variations in the flowfield discussed.

4.1.1 Validation and Characterization of Stereo-Vision Measurements

In order to ensure that the stereo-vision system is performing as expected, a simple cross-validation with the tip encoder is conducted. Figure 7 presents the time-history of the local angle of attack at four spanwise locations measured by the stereo-vision system plotted with the wing tip angle of attack measured by the cyber-physical system's optical encoder.

From these results a very close agreement is observed between the cyber-physical predicted tip angle of attack (tip-twist angle) and the stereo-vision angle of attack at 98% span. The signals match exceptionally well in phase, but display small deviations in the peak amplitude up to $\Delta\alpha = 2^o$. While this deviation is on the order of the measurement uncertainty in the stereo-vision system as reported in Section 3.6, it appears to be a systematic error in the experiment. Specifically, the stereo-vision data consistently under-measures the peak angle of attack in the positive direction, while consistently over-measuring the negative peak. This suggests that there is a small bias between the $\alpha = 0^o$ positions in the cyber-physical and stereo-vision measurement systems on the order of $\delta(\alpha) \approx 0.5^o$. Additionally the larger discrepancy at the positive peaks may also be due to the exacerbation of the stereo-vision measurement uncertainty with greater distance away from the cameras. Specifically, note that there is similar phasing between the twisting and bending modes of the wing; thus as the wing reaches its maximum angle of attack, $\alpha_{Tip} = 30^o$, the surface also reaches its maximum bending deflection. All that said, the agreement validates the captured stereo-vision data within the confidence of the measurement systems.

At the given testing conditions, noted in Section 3.4, the cyber-physical wing system underwent a very periodic oscillation. This is easily observed through examination of the cyber-physical data and the processed stereo-vision motion as was shown in Figure 7. The tip notably followed a sinusoidal-like motion with a frequency of $f = 5.4\ Hz$ and an amplitude of approximately 15° centered at $\overline{\alpha_{Tip}} = 14.5^o$. It should be noted that the wing root angle of attack was fixed at $\alpha_{Root} = 10^o$, thus the tip on average displayed a 5° washout relative to the root position.

Further visual examination of this limit cycle oscillation presented in Figure 7 shows that the pitching oscillation is dependent on spanwise position. This is indicative of the spanwise gradients expected from the flexible (or deformable) wing model. It is also apparent that the pitching motion is biased towards positive angles of attack. Specifically, the pitch angle oscillates from $\theta = -5^o$ to $\theta \approx 30^o$ with respect to the root angle of attack (i.e. the root referenced twist angle).

4.1.2   Periodicity and Cycle Variation in the Wing Deformation

Before discussing the modal analysis, the variability in the stall flutter oscillation is understood. To visualize this variability, a cycle to cycle overlay of the pitching and the bending signals at the tip location across the entire $20\ s$ period is provided in Figure 8. Additionally in Figure 8a, a sine wave is plotted for reference on top of the tip-twist data (dashed red line). This clearly demonstrates a noticeable distortion of the trajectories from a pure sinusoidal motion. For the tip-twist data, this results qualitatively in the sharpening and broadening of the positive and negative peaks in the cycle respectively. The influence of the secondary frequency is even more apparent in the bending overlay, where secondary oscillations appear to be superposed on-top of the primary frequency. From this overlay, the variability in amplitude is qualitatively observed to be on the order of $\Delta\theta \approx \pm 3^o$ and $\Delta T_y < \pm 10\ mm$.

The cycle to cycle variability in frequency or phase is demonstrated when taking the autocorrelation of the raw x, y displacement data. Figure 9 presents the normalized, autocorrelation in time for each of the torsional and bending displacement time-series, and strongly demonstrates the wandering of the kinematics through the testing window. Each

(a) Torsion   (b) Cross-stream Bending
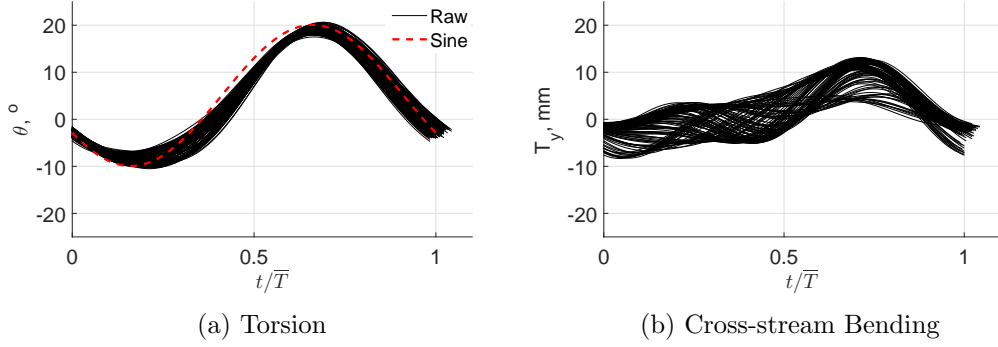
Figure 8: Cycle-to-cycle variability present in data as shown by overlaying each individual cycle of the 20 s data capture period (approximately 105 cycles) for (a) the torsional deflection, θ, with sine wave plotted for reference, and (b) the cross-stream bending, T_y.

of the displacements remain highly correlated within the first two seconds of the full 20 s period, implying that the LCO is stable and highly periodic for approximately 11 cycles. However after the initial 2 s a significant reduction in correlation value is observed, indicating that the kinematics are wandering away from the initial state. At approximately the 4 s mark the correlation drops to near zero values. Since the cycle-to-cycle overlay data presented previously in Figure 8, does not show a very large change in waveform shape, it is inferred that this decrease in correlation represent changes in frequency or phase and amplitude as time progresses.

Figure 10 shows phase plane plots, where the bending deflection is plotted against the torsional deflection for three limit cycles. This data shows that the wing motion clearly follows a repeated, limit cycle trajectory with a significant hysteresis that grows uniformly with spanwise position. It also demonstrates the wandering in the limit cycle trajectory that was previously discussed. As a note, plotting over more cycles would also show an increase in variability for this figure.

From this data, the maximum phase-averaged cross-stream bending deflection, T_y, appears to correlate closely with the maximum pitch angle, θ, at each spanwise position. Running a cross-correlation indicates a phase lead in the bending signal of $\Delta t/T = 0.032$ (or a phase angle of $\gamma = 11.5^o$ in the average cycle). This can potentially be explained when considering the aerodynamic force production. The largest lift force will occur near the maximum angle of attack just before the flow field fully separates and the wing stalls. Additionally, the wing's bending response time is expected to be much faster than its torsional response time owing to its lower torsional natural frequency as compared with bending. Thus it is inferred that the maximum bending deflection correlates closely to the stall point, but that the torsional motion persists beyond the stall point. This is potentially due to the lower torsional stiffness of the system, but could also be related to cycle differences in the maximum lift and pitch moment production; which requires further investigation. Even so the structural LCOs are primarily dominated by the stall aerodynamics of the wing; as previously observed with stall flutter [Dimitriadis and Li, 2009, Razak et al., 2011, Tang and Dowell, 2001, 2002].

Finally, it should be noted that the wing was designed to be torsionally weak, but strong in bending to effectively decouple the modes. As shown in the preceding results, the bending

(a) Torsion

(b) Cross-stream Bending
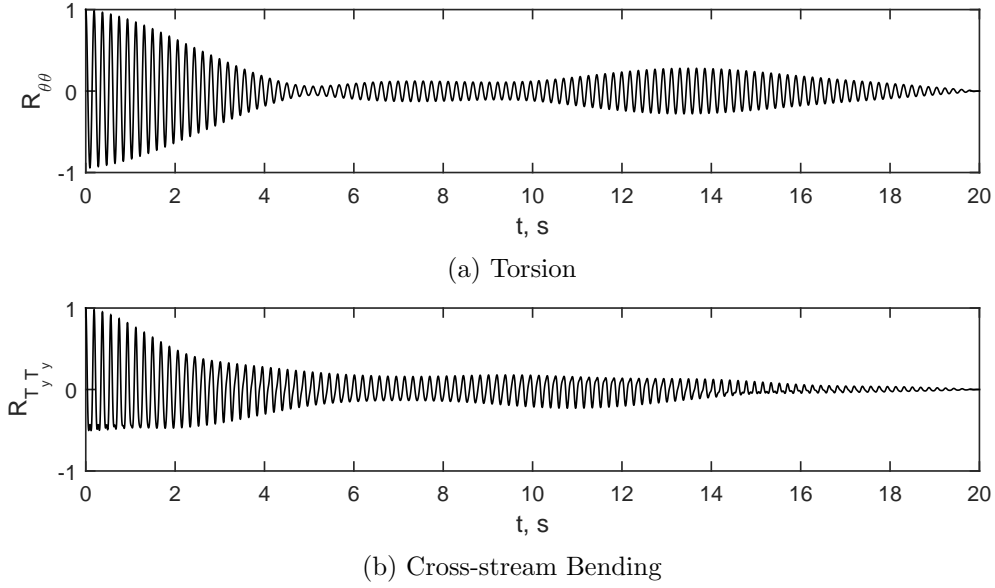
Figure 9: Autocorrelation in time of the (a) torsional displacement, θ and (b) cross-stream bending displacement, T_y signals.

signal is not fully decoupled. This is because the model has finite stiffness in bending and as discussed previously, the aerodynamics produce a maximum lift force near the maximum pitch angle. With that said, the 2 cm bending deflection is quite small in comparison to the 30° pitching amplitude, indicating that the wing is dominated by the torsional motion, as intended.

4.1.3   Fourier Decomposition of the Wing Deformation

Evidence of a single (or first) mode dominance appears in the spectral analysis of the pitching and bending signals presented in Figures 11 and 12 where a fast Fourier transform (FFT) was applied to the torsion and cross-stream bending for each of the spanwise positions independently. Note that the number of samples used in the FFT was 16384 ($T \approx 16\ s$) at a sampling frequency, $f_s = 1\ kHz$ thus the frequency resolution in the plots are $\Delta f = 0.061\ Hz$. In both of the plots, a dominant frequency of $f = 5.4\ Hz$ and second frequency at $f = 10.7\ Hz$ (approximately twice that frequency) are observed in both signals though there is some broadening of the FFT peaks. This is likely a result of the frequency variation discussed previously. The dominant frequency matches closely to the expected torsional natural frequency of the flexible wing system, which is estimated to be to be $\omega_\theta = 5.66\ Hz$ using the prescribed properties of the cyber-physical system (Section 4.1) and Equation 7 for a second-order linear dynamic system. The observed second frequency, $f = 10.7\ Hz$, distorts the torsional motion away from a pure sinusoidal oscillation, inducing the peak sharpening/broadening observed in Figure 8a. Furthermore, no oscillations are observed around the primary frequency since the secondary frequency is only twice that of the primary.
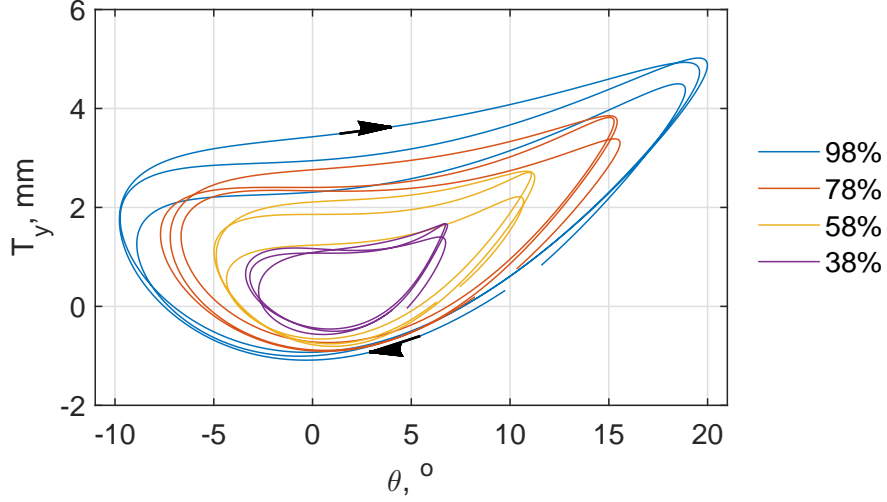
Figure 10: Phase-plane plot of T_y bending deflection versus torsional deflection angle, θ, at spanwise locations of $z/b = 1, 0.78, 0.58$, and 0.38, over three limit cycle periods.

$$\zeta = \frac{\eta}{2\sqrt{k_\theta J}} \tag{6}$$

$$\omega_\theta = \frac{1}{2\pi}\sqrt{\frac{k_\theta}{J}(1 - \zeta^2)} \tag{7}$$

Plotted alongside the frequency-amplitude spectrum for each signal at each spanwise location is a frequency-phase plot. In the torsion signal, this plot shows that the first frequency components have matching phase angles while the second frequency component shows a significant variation in phase. The phase locking of the dominant frequency indicates that the wing motion for that frequency can be described by a single, continuous mode shape oscillating with the same sinusoidal trajectory. The variability in the calculated phase angle for the second frequency is more likely an indication of data noise as the associated amplitudes for this fourier component are quite small, though as will be shown later they are still significant. Subsequently, all wing sections are considered to move torsionally in-phase.

Examining the phase of the bending signal indicates two frequencies are also present however they share similar dominance. Furthermore, the phase angles for both of the frequencies match closely; which may further enforce the argument that the phase variation in the second torsional frequency is more a result of small amplitude signals than a physical effect. Also note in all of these decompositions, the fourier spectrum shows a significant non-zero mean which validates that the wing oscillates around a position different from the base angle-of-attack. Additionally, since this mean offset is positive, the wing favors positive deflection.

Finally, it should also be noted that the bending natural frequency of a nearly identical flexible wing system was measured to be $\omega_h = 11.45\ Hz$ by Fagley et al. [2016]. This frequency closely matches the second dominate frequency peak observed in the data and may also explain why this frequency appears stronger in the bending spectrum. That
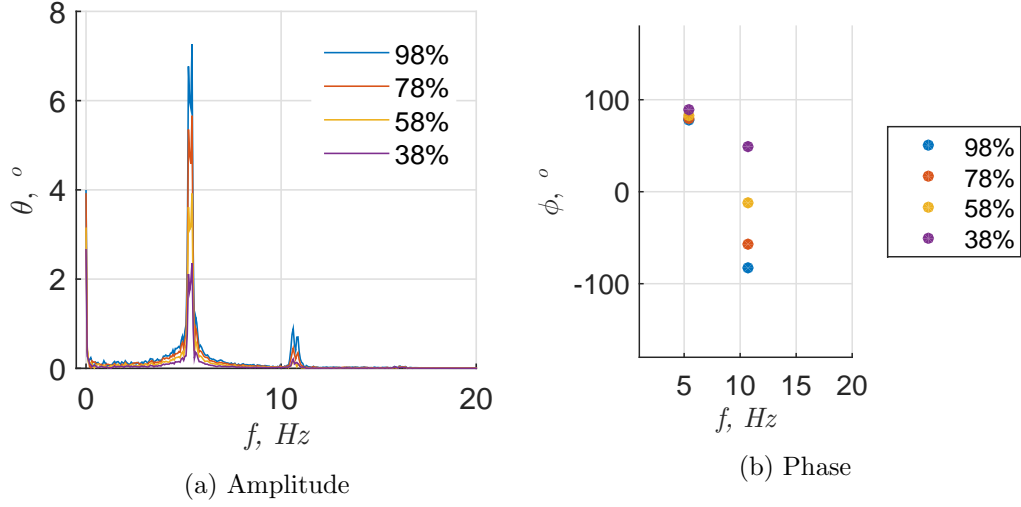
(a) Amplitude

(b) Phase

Figure 11: Comparison of a) amplitude and b) phase of spectral (FFTs) analysis of Torsion signal projected to rigid body.
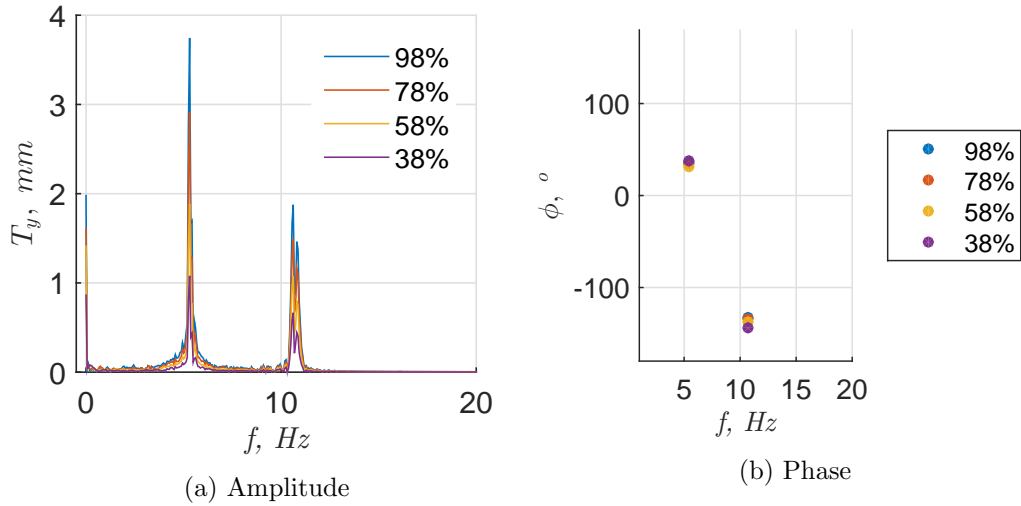
(a) Amplitude

(b) Phase

Figure 12: Comparison of a) amplitude and b) phase of spectral (FFTs) analysis of cross stream bending signal projected to rigid body.

said the first torsional frequency still dominates the spectral content, with no observable frequencies related to the higher order torsion or bending eigenmodes. Note that these would theoretically be expected to appear at $\omega_{\theta_{mode2}} = 3\omega_\theta$ and $\omega_{h_{mode2}} = 6.3\omega_h$, respectively for a cantilevered beam in free vibration [Hodges and Pierce, 2014]. It is however possible, that due to spatial aliasing across the wing, these frequencies are not observed in the FFT.

4.1.4   Eigenfunction Projection of the Wing Motion

From the Fourier expansion it is expected that a single dominant mode (in the frequency domain) will appear in the torsional motion, potentially oscillating sinusoidally. In contrast for the bending motion two equally dominant modes are expected. Therefore to provide a more descriptive decomposition of the wing motion, in the time domain, the eigenfunction solutions for a cantilevered beam are utilized. This was accomplished through projecting the measured unsteady torsion and bending deflections onto the first three analytically predicted mode shapes for a clamped-free beam in both torsion and bending vibration. While the Fourier expansion doesn't show frequency peaks associated with higher modes, three eigenmode shapes are utilized to ensure that the non-linearities in the wing motion can be best captured. The unsteady (time-varying) mode weights associated with these modal projections are plotted in Figures 13 and 14 for the torsional component, θ, and the cross-stream bending component, T_y, respectively. Note that the Fourier decompositions of each of the unsteady mode weights are also plotted in these figures.

The torsional time-varying mode weights, Figure 13a, similarly display the dominance of the first torsional mode in the wing motion. Specifically, the first mode displays the largest amplitude, as compared with the amplitudes of the second and third modes which are nearly an order of magnitude smaller. Therefore, the majority of the motion is derived from the first eigenmode with the second and third potentially capturing the small, time varying perturbations around this principle mode.

As with the torsion modes, Figure 14a presents the time-varying bending mode weights. The bending deflection shows a similar dominance in the first mode, however the second and third modes show more significant weight than was observed in the torsional motion. The bending deflection also shows a changing amplitude through the 20 s window that may be consistent with a low frequency beat. It is reasonable to expect a beat to form in the bending signal, because as noted previously, the second frequency in the FFT spectrum is very near to the expected natural frequency of the wing in bending.

As expected, the spectral content of the modes, in each the torsion and bending directions, matches closely to that of the data prior to projection onto the theoretical eigenmodes (Figures 11 and 12). Furthermore, the first mode clearly dominates the frequency content, though the second mode does have greater importance in the bending signal.

This analysis demonstrates that within the 20 s windows, the waveform shape is accurately represented by the eigenmode decomposition which is also able to capture the wandering of the signals over time. Since the loss in correlation is attributed to small frequency and amplitude variations, as discussed in Section 4.1.2, rather than fundamental changes in waveform shape, these modes can be generalized and expected to describe the motion for an arbitrary window size. Most notably, the linear mode shapes accurately capture the nonlinear wing response in both bending and torsion.

Taking this approach, the non-linearities appear in the time-varying modal weights

(a) Torsional Mode Weights
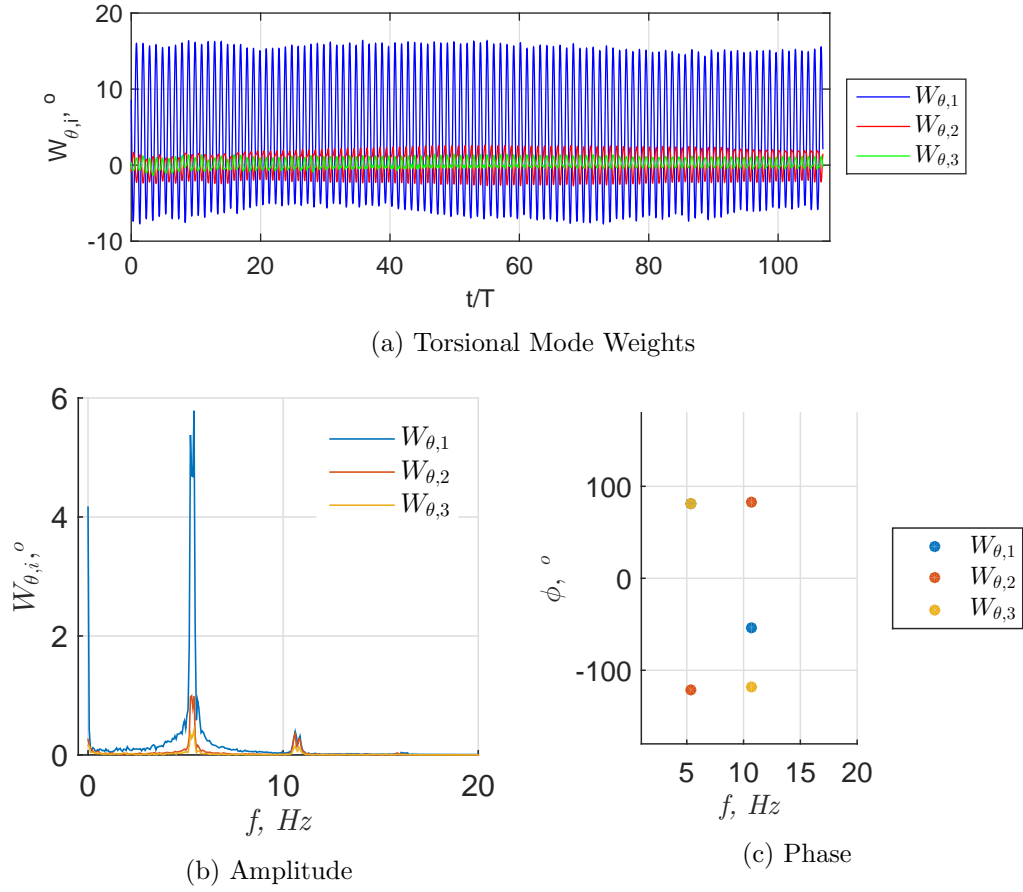
(b) Amplitude

(c) Phase

Figure 13: Comparison of a) torsional mode weights b) amplitude and c) phase of spectral (FFTs) analysis of Torsion eigenmode signal for first three modes.

(a) Bending Mode Weights
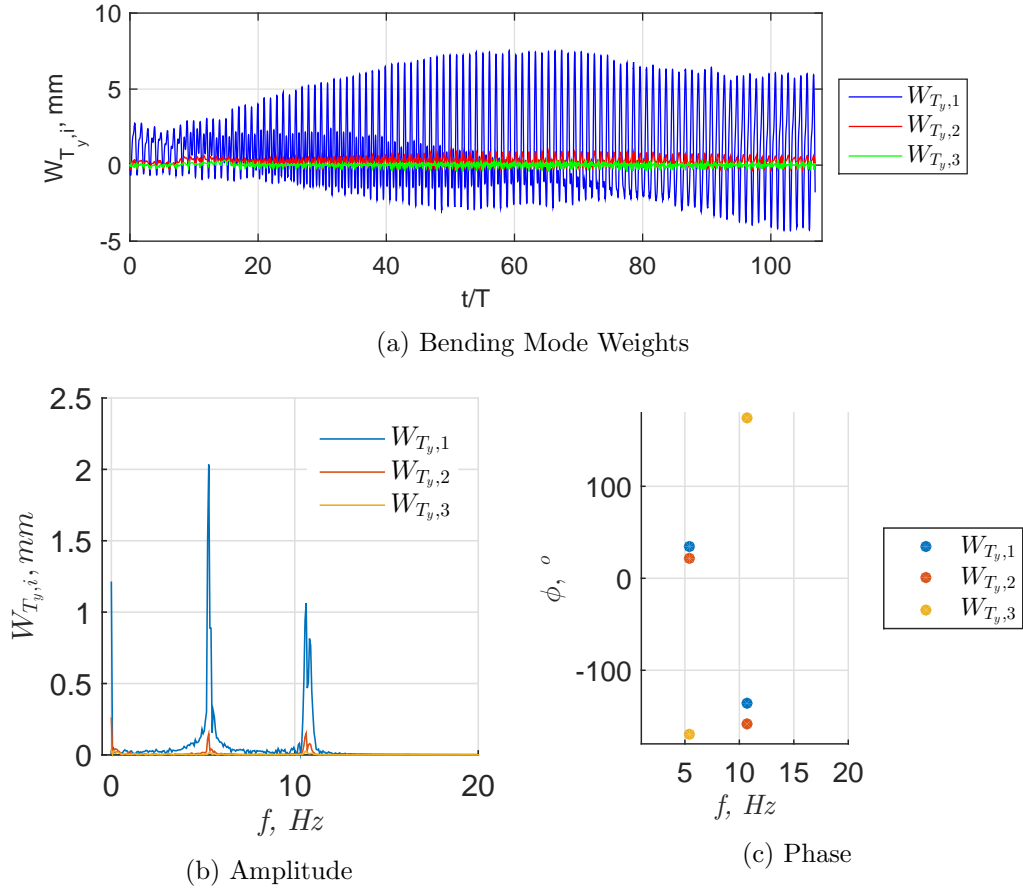
(b) Amplitude

(c) Phase

Figure 14: Comparison of a) bending mode weights b) amplitude and c) phase of spectral (FFTs) analysis of bending eigenmode signal for first three modes.

associated with each mode. However, with the dominance of the first mode, in the torsional deflection and the relatively small bending deflection, the wing deformation can be largely constructed by the first mode in torsion and its associated weight. For completeness, the next section will determine weights associated with each of the modal components.

4.1.5 Kinematic Equations

Based upon the eigenmode projection and the fundamental frequencies present in the data, an empirically defined kinematic relation can be written for the stall flutter motion observed.

In the torsional direction (Figure 13), the second frequency at $10.7 \ Hz$ is relatively small in amplitude as compared to the first (dominate) frequency, however its presence is still significant. Specifically, it was previously shown that the motion is not purely sinusoidal and thus the second frequency influences the asymmetry, or peak broadening/sharpening, across the cycle. Additionally, the higher order modes are retained to potentially capture spanwise non-linearities in the wing. Also note that inspection of the phase plot (Figure 13c) shows that the second and third modes are nearly 180° out of phase for the torsional component. However this does not imply cancellation of these modes, as they represent orthogonal shapes whose spatial dependencies are also 180° out of phase.

In contrast, the Fourier decomposition of the bending mode weights (Figure 14) shows that the two frequencies share similar levels of dominance in both the first and second modes of bending. However the third mode shows no significant spectral content, thus it will be ignored in the mathematical model of the bending motion.

The kinematic equations of motion for the wing are thus written in terms of both the eigenmodes, which prescribe the spatial dependencies, and the Fourier series components at the identified frequencies, which prescribe the time dependence. The resulting relationships are defined by Equations 8 and 9. These equations are consistent with previous work in that they isolate the motion to a principally torsional oscillation (one degree of freedom), but allow for small bending components to couple in. In contrast to previous works, the kinematic relation shows the presence of two frequencies indicating that the stall flutter motion is not restricted to a pure sine wave in a deformable wing body.

$$\theta(z,t) = \sum_{i=1}^{3} \left(\overline{W_{\theta,i}} + \sum_{j=1}^{2} [a_{ij} cos(2\pi\omega_j t) + b_{ij} sin(2\pi\omega_j t)] \right) \psi_{\theta,i}(z) \tag{8}$$

$$T_y(z,t) = \sum_{i=1}^{2} \left(\overline{W_{T_y,i}} + \sum_{j=1}^{2} [c_{ij} cos(2\pi\omega_j t + \gamma) + d_{ij} sin(2\pi\omega_j t + \gamma)] \right) \psi_{Ty,i}(z) \tag{9}$$

For the current experimental data, all of the empirical coefficients were determined through a least squares fit across the full $20s$ period of the data set. Note that the fundamental frequencies were found to be $\omega_1 = 5.4 \ Hz \pm 0.20 \ Hz$ (torsion) and $\omega_1 = 5.4 \ Hz \pm 0.59 \ Hz$ (bending) and $\omega_2 = 10.7 \ Hz \pm 0.31 \ Hz$ (torsion) and $\omega_2 = 10.7 \ Hz \pm 0.59 \ Hz$ (bending). The remaining coefficients are included in Tables 1 and 2 for the torsion and bending components, respectively. The mean coefficients as well as the standard deviations from these values are included in the tables. Also note that the phase shift between the bending and torsional signals is captured in the variable γ, and was found to be $\gamma = 11.5^o$,

Table 1: Empirical coefficients for the torsional kinematics, $\theta(z,t)$ (Equation 8).

$\overline{W_{\theta,1}}$	4.3 ±0.25	$\overline{W_{\theta,2}}$	0.28 ±0.19	$\overline{W_{\theta,3}}$	0.17 ±0.14
a_{11}	-5.2 ±0.68	a_{21}	0.50 ±0.40	a_{31}	-0.35 ±0.13
a_{12}	-0.072 ±0.22	a_{22}	0.26 ±0.18	a_{32}	-0.11 ±0.10
b_{11}	-9.6 ±0.79	b_{21}	1.9 ±0.30	b_{31}	-0.65 ±0.12
b_{12}	0.18 ±0.28	b_{22}	-0.45 ±0.23	b_{32}	0.17 ±0.12

Table 2: Empirical coefficients for the cross-stream translation kinematics, $T_y(z,t)$ (Equation 9).

$\overline{W_{T_y,1}}$	1.2 ±0.65	$\overline{W_{T_y,2}}$	0.26 ±0.054
c_{11}	-0.57 ±1.7	c_{21}	-0.09 ±0.10
c_{12}	-1.0 ±0.76	c_{22}	-0.19 ±0.09
d_{11}	-2.3 ±1.8	d_{21}	-0.16 ±0.12
d_{12}	0.33 ±1.06	d_{22}	0.023 ±0.10

with the torsional signal lagging the bending. The tabulated values in Tables 1 and 2 are consistent with previous arguments that the pitching motion is dominated by a single torsional mode with slight perturbations from higher order modes as demonstrated by their small magnitudes.

The mean wing trajectory is reconstructed and compared to the raw cycle to cycle data for the full $20s$ period in Figures 15 and 16 utilizing the empirically determined kinematic relations for the torsional (Equation 8) and bending (Equation 9) motions, respectively. Note, that for the torsional component (Figure 15) a progression of modal reconstructions are presented including: (1) only the dominate (θ_1), (2) the first two ($\theta_1 + \theta_2$), and (3) all three eigenmodes ($\theta_1 + \theta_2 + \theta_3$). All three reconstructions of the torsional motion qualitatively capture the cycle to cycle mean to approximately 80% for the full model span. That said, it is clear that utilizing only the first, dominate eigenmode causes the tip amplitude ($z/b = 98\%$) to be under-predicted, while significantly over-predicting the amplitude at $z/b = 38\%$. Progressively including the additional eigenmodes allows the model to better capture the spanwise non-linearity, but with diminishing returns.

Greater deviations from the raw data are visible in the reconstruction of the mean bending signal (Figure 16). This may be the result of a greater variation between the cycles across the data period, which would skew the mean coefficients. With that said, the coefficients can be individually fit to any individual cycle allowing for a nearly exact recreation of that cycle. However further work would be required to better adapt this approach to a fully deterministic, predictive model for the entire time history (20 s period). More specifically, a model that accurately describes the time dependent phase and amplitude variability across the data set would be required. Thus the primary limitation of the current approach lies within the independent (non-linear) weightings of each eigenmode. While this allows the empirical model to be adapted to non-linear variations in the wing motion, it limits the predictive ability of the model. With that said the results show that the torsional deflection can be predicted across the span to approximately 80% accuracy by the first torsional mode alone. Thus for some in-situ applications it may be sufficient to predict the

(a) 98%
(b) 78%
(c) 58%
(d) 38%
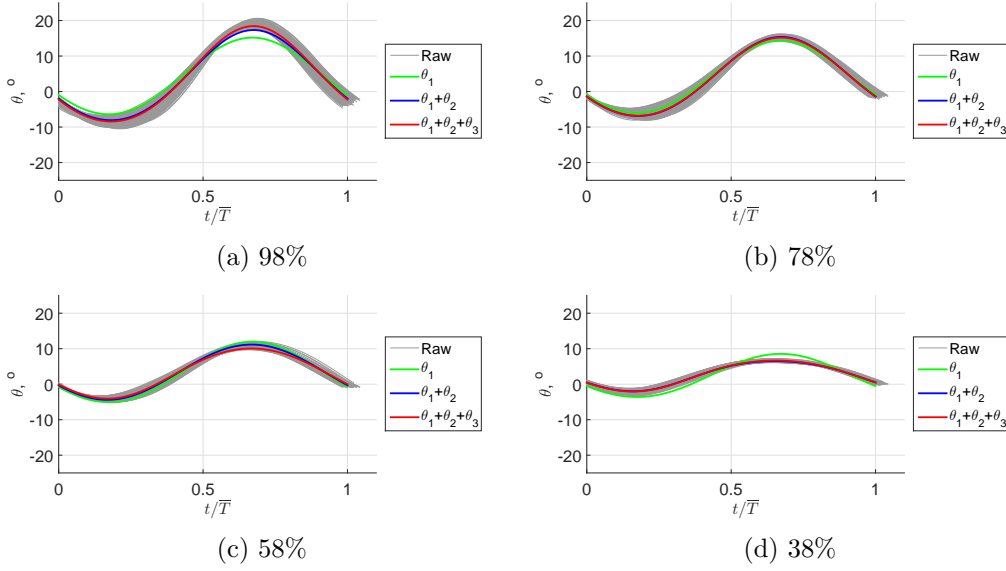
Figure 15: Comparison of the raw and reconstructed trajectories in θ for each spanwise measurement location.

spanwise deformation from only the first mode.

4.1.6 Integrated Torque Prescribed by Cyber-Physical System

To gain some insight into the development of forces around the flexible, finite span wing, the moment developed at the wing tip due to the flowfield was calculated using the method discussed in Section 3.8. As was discussed previously, this tip torque is not the aerodynamic pitching moment as would be measured at the wing root, but is rather related to the net deflection of the wing tip resulting from all aerodynamic pitching moments integrated along the surface of the wing. This tip moment is normalized and presented as a moment coefficient using $C_m = \tau_{tip}/qSc$. In the proceeding analysis, two data cases are analyzed where the first corresponds to the stereo-vision data published in Culler et al. [2017], where $k_\theta = 0.47 \ N \ m \ rad^{-1}$, $\eta = 6.09 \times 10^{-3} \ N \ m \ s \ rad^{-1}$, and $J = 4.25 \times 10^{-4} \ kg \ m^2 \ rad^{-1}$. The second corresponds to the structural properties during the SPIV testing and are $k_\theta = 0.54 \ N \ m \ rad^{-1}$, $\eta = 5.0 \times 10^{-3} \ N \ m \ s \ rad^{-1}$, and $J = 4.25 \times 10^{-4} \ kg \ m^2 \ rad^{-1}$. These cases will be subsequently referred to as the stereo-vision and SPIV cases, respectively. In both data sets, the same wing model was tested at the same tunnel velocity of $U_\infty = 26$m/s. Because the same model was utilized and the virtual inertia J_V was left constant, the inertia was the same for each test case. The stiffness and damping were varied slightly between the cases by $0.07 \ N \ m \ rad^{-1}$ and $1.09 \times 10^{-3} \ N \ m \ s \ rad^{-1}$ respectively, where the first case had lower stiffness but higher damping and the second had higher stiffness but lower damping. These structural properties were estimated through system identification of the model's response to a step input as described in Fagley et al. [2015].

The calculated C_m is plotted against the tip trajectory in Figure 17 for both cases, showing a clear hysteresis loop. The figure shows that both C_m versus θ loops have similar character however the case corresponding to the SPIV data (red) reached a negative angle
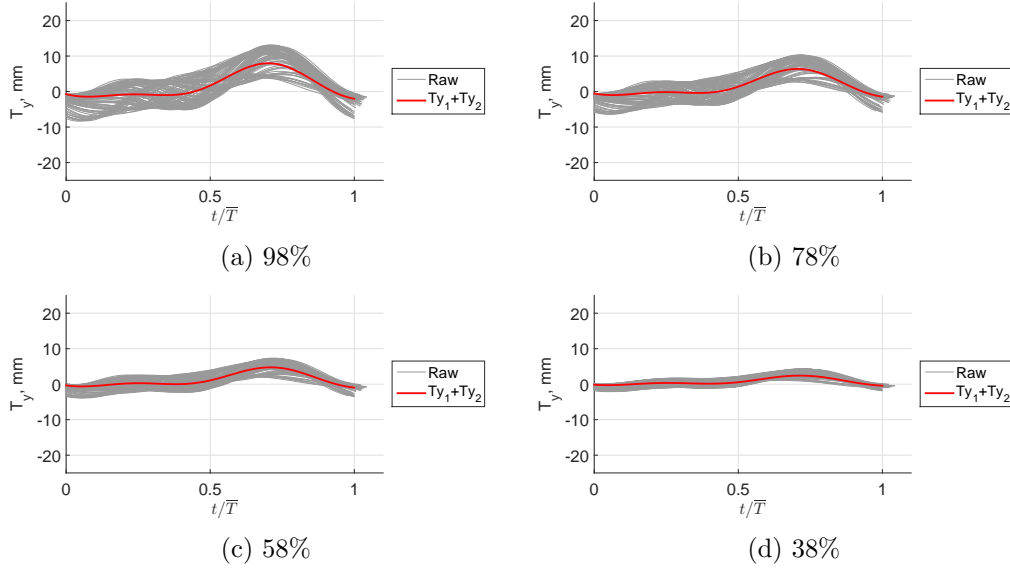
Figure 16: Comparison of the raw and reconstructed trajectories in T_y for each spanwise measurement location.

of attack approximately 4° lower than the stereo-vision case (grey). This is consistent with the lower structural damping in the SPIV case which is expected to allow for larger amplitude pitch oscillations. In both cases, the pitch-up portion of motion was characterized by positive torques and the pitch down motion by small, negative net torque. This implied that the integrated aerodynamic pitching moment along the wing largely goes to zero and that the wing angular position is restored primarily due to the internal structural forces. This further suggests that the wing was fully stalled during the pitch down portion of the motion. This significant decay in the pitching moment is also consistent with the general expectations of dynamic stall, where the lift force significantly drops after a stall condition is reached. It should also be noted that the wing reached a maximum tip angle of attack of $\alpha_{max} \approx 30^o$ ($\theta_{max} \approx 20^o$) for both the stereo-vision and SPIV cases. An angle of attack of 30° is significantly higher than the static stall angle of 19° as presented in Goett and Bullivant [1938] and reaching this high angle of attack before stall is consistent with classic descriptions of dynamic stall [Larsen et al., 2007, Leishman and Beddoes, 1989].

From the calculation of internal pitching moment, the stability of the coupled system can be determined through calculation of differential aerodynamic work as discussed byMcCroskey [1981]. Specifically, the direction of the differential work, $dW = -C_m d\alpha$ will indicate whether the structure is doing work on the flow or whether the flow is doing work on the structure. In the case of positive dW the structure is doing work on the flow and the system is stable. In the case of the negative dW the fluid is doing work on the structure and the system will tend towards instability, or growth of LCO amplitude.

A plot of dW versus tip-twist angle, θ, is provided in Figure 18. The figure shows that the peak negative dW is approximately 17% larger for the SPIV case (red) than for the stereo-vision case (grey). This is again consistent with the lower structural damping, which creates a less stable configuration. From the figure, it is further observed that the dW becomes positive at the turning points or maximum and minimum twist angles. This also
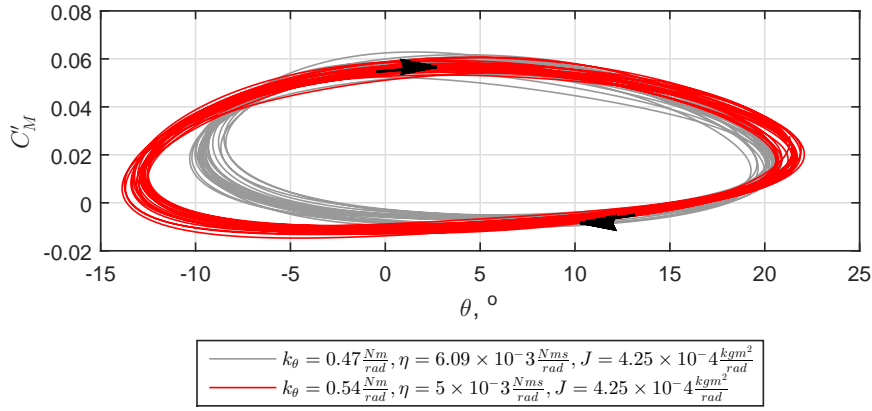
Figure 17: C_m versus tip-twist angle, θ, loops for the stereo-vision case (grey) and the SPIV case (red).
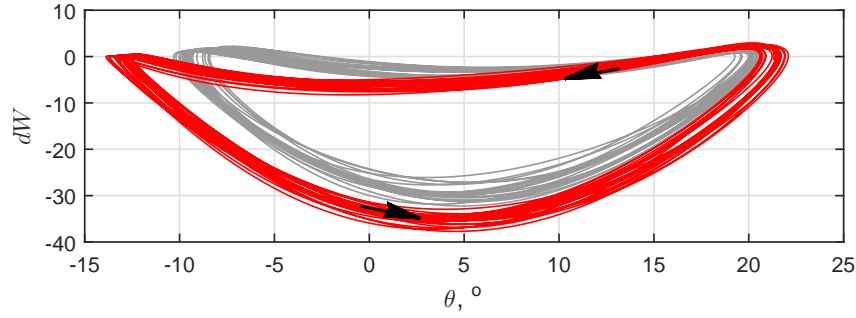
Figure 18: The differential work dW versus tip-twist angle, θ for the stereo-vision case (grey) and the SPIV case (red).

makes sense as it indicates that the stabilization of the system provides the bounds on the amplitude of oscillation. From the dynamic stall perspective as discussed previously, this maximum amplitude boundary is likely associated with wing stall. Furthermore, during the majority of the cycle, dW is negative indicating that the aerodynamics are dominating the structural response as was observed by Tang and Dowell [2001, 2002].

From these results it becomes clear that the observed stall flutter LCO exhibits a delay of stall behavior that is likely attributable to a dynamic stall event. Furthermore, the results show that the pitching amplitude maxima is associated with a re-stabilization of the system. This stability bound is likely associated with stall of the wing. With this information, stereo particle image velocimetry data was collected near the peak angle of attack, encompassing the phase region where flow separation occurs. These phases where selected to determine whether a dynamic stall vortex develops and interacts with the wing surface as is the case in rigid body motion.

(a) Angle of Attack   (b) Pitching Moment
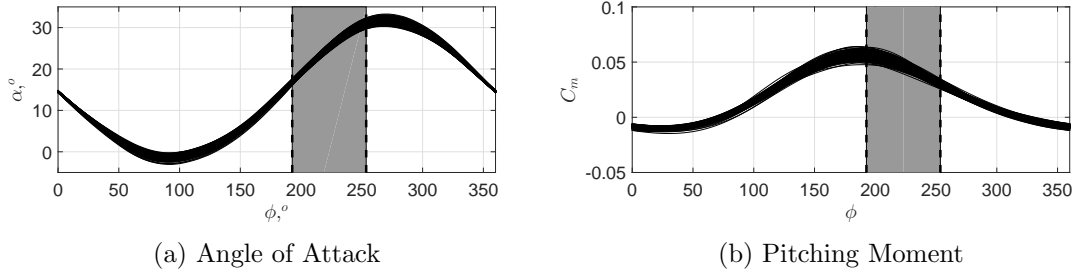
Figure 19: Phase locations of SPIV data collection relative to the (a) wing tip angle of attack and (b) internal pitching moment.

4.1.7   Flow Field Measurements

In order to understand how flow separation evolves along the wing, stereoscopic particle image velocimetry measurements where taken at the spanwise and phase locations noted in Section 3.7. Specifically, a phase sweep at $z/b = 0.75$ is presented, corresponding to the approximate spanwise location of maximum separation. SPIV planes at additional spanwise locations of $z/b = 0.58$, 0.625, 0.71, 0.75, 0.79, and 0.875 are presented to determine whether or not the stall flutter flowfield was characterized by widespread or localized separation. All of the captured phase locations for each spanwise position are located within the region illuminated in Figure 19.

As the figure shows, the SPIV phases start at the approximate peak in C_m and progress through the region of decreasing C_m. As a note, despite the general trend of decreasing C_m, all of the SPIV phases correspond to pitch up motion of the wing, as also demonstrated in Figure 19. Thus the maximum C_m occurs well before the wing reaches maximum pitch angle.

The results for the phase sweep at $z/b = 0.75$ are presented in Section 4.1.8 while the results for the spanwise sweep are presented in Section 4.1.9. For the phase sweep at $z/b = 0.75$ select phases are presented, interspersed across the measurement window, to show the principle features of separation for the flexible wing.

4.1.8   Phase Evolution of the Flow Field

Figure 20 presents streamlines overlaid on normalized vorticity contours, $\Omega_Z \frac{c}{U_\infty}$ for phases angles of $\phi = 185^o$, 200°, 216°, 224°, 231°, and 243° at $z/b = 0.75$. Note that in these figures the vorticity and streamlines were computed from phase-averaged velocity fields. From the figure it is clear that the maximum C_m occurred during predominantly attached flow. This is exemplified by Figure 20a where $\phi = 185^o$ which shows that the flow is effectively attached across the entire wing chord. Stepping forward in phase to Figure 20b, the phase-averaged fields begin to show trailing edge initiated separation which is consistent with the stalling behavior of a relatively thick airfoil profile such as the NACA 0018 utilized here. By $\phi = 216^o$, shown in Figure 20c, the flowfield shows significant re-circulation near the trailing edge, which reaches the leading edge by $\phi = 243^o$. While the flowfield streamlines began to resemble a dynamic stall (leading edge) vortex when $\phi = 243$ this resemblance was not indicative of such a vortex existing for two reasons. First, the separation was trailing edge initiated. In classical discussions of dynamic stall the vortex forms from leading edge

initiated separation Larsen et al. [2007]. This is often argued to be the result of a leading edge separation bubble bursting event, however in this case, no leading edge separation bubble forms. Second potential flow arguments can be made to explain why a coherent leading edge vortex does not form by noting a particular aspect of the wing deformation. Specifically, as noted in Culler et al. [2017], the wing deforms in a spanwise varying fashion largely defined by the first eigenmode for a cantilevered beam. This means that at the wing root, the airfoil is at the geometric or base angle of attack of $\alpha = 10^o$, where stall and large scale separation does not occur in static tests. Therefore, for a leading edge vortex to exist near the 75% span location, the vortex filament would be required to terminate within the fluid, a clear violation of Helmholtz second theorem or on the wing body. Clearly to satisfy Helmholtz theorem, any formed vortices have to bend into a U-shape thereby terminating at the wing surface.

The argument that no dynamic stall vortex is present is further supported by the instantaneous fields. Specifically, in Figure 21, streamlines are again plotted, however they are overlaid on contours of the Q-criterion which is discussed by [Hunt et al., 1988] and is determined from $Q = 1/2(|\Omega^2| - |S^2|)$ [Jeong and Hussain, 1995]. In the plots red contours indicate regions of positive Q and therefore high rotation while blue contours indicate negative Q and therefore high shear. Note that the figure shows a sequence of "representative" instantaneous flowfields from the previously presented phase-averaged sets. Consistent with the phase-averaged results of Figure 20 the streamlines show a region of re-circulation beginning at the trailing. However, when examining the resulting Q fields, it becomes clear that the flow consists of small scale structure consistent with a separated shear-layer, rather than a coherent dynamic stall vortex. Note, in these fields Q_{rms} is approximately $1.5(10^6)$.

When the remaining instantaneous fields are analyzed and the size and location of the concentrations of Q are compiled (not shown here), it becomes even more apparent that the only small structures are observed randomly distributed along a shear layer emanating from the suction surface of the airfoil. In fact there is no coherently identifiable dynamic stall vortex in any of the phases. As a result, the wing stall can be associated with trailing-edge initiated shear layer separation rather than the formation of a large structure as is typically observed in rigid body models. Furthermore, the lack of visible periodicity in the spatial locations of the small scale structures implies that the shedding of the these structures within the shear layer is not coupled or locked to the the frequency of the LCO. As will be discussed in Section 4.1.9 this trailing-edge initiated shear layer separation is concentrated in only the outer 2/3 span of the flexible wing.

4.1.9   Spatial Variation of the Flow Field

As was shown in Section 4.1.8, the flow separation is defined by trailing-edge initiated shear layer separation rather than the formation of a coherent, large scale structure initiating leading separation. In order to understand how this varies along the span, the flowfield was also studied at span locations from $0.58 < z/b < 0.875$ and at $\phi = 204^o$, 214°, and 224°. Figure 22 presents the phase-averaged flow field for along the span for a phase angle of $\phi = 224^o$, where streamlines are plotted overlaid on contours of vorticity. The figure shows that the extent of flow separation along the wing chord is dependent upon spanwise location. At the locations $z/b = 0.58$ and 0.875 as shown by Figures 22a and22f, respectively, the extent of flow separation is significantly reduced compared to $z/b = 0.75$.

(a) $\phi = 185^o$

(b) $\phi = 204^o$

(c) $\phi = 214^o$

(d) $\phi = 224^o$

(e) $\phi = 231^o$

(f) $\phi = 243^o$

Figure 20: Streamlines overlaid on contours of normalize vorticity, $\Omega_Z \frac{c}{U_\infty}$, for the phase-averaged flowfields around flexible wing at $z/b = 0.75$ for phase angles from $\phi = 185^o$ to $\phi = 243^o$.

(a) $\phi = 185^o$

(b) $\phi = 204^o$

(c) $\phi = 214^o$

(d) $\phi = 224^o$

(e) $\phi = 231^o$

(f) $\phi = 243^o$

Figure 21: Streamlines overlaid on contours of Q for instantaneous flowfields around the flexible wing at $z/b = 0.75$ for phase angles from $\phi = 185^o$ to $\phi = 243^o$.

Furthermore, at $z/b = 0.875$, the flow appears to be fully attached. This tendency towards flow reattachment is argued to be the result of two effects depending upon the spanwise location.

At inboard spanwise positions the linear variation in the wing twist angle reduces the effective angle of attack thus reducing the severity of flow separation. Specifically, the wing root is fixed to an angle of attack of $\alpha = 10^o$ which corresponds to statically attached flow. Because of the twist distribution noted in Culler et al. [2017], span locations closer to the root will also be at statically attached angles of attack. Using the first eigenmode to estimate this twist angle at the spanwise location $z/b = 0.58$ for the phase angle $\phi = 224^o$ it is found that the angle of attack is expected to be $\alpha = 20.15^o$ based upon the tip twist noted in Figure 19. Using the surface reflection measuring technique from the SPIV data, the angle of attack at this location was measured to be $\alpha = 20.4^o$. This angle of attack is near the static stall angle for a NACA 0018 wing [Goett and Bullivant, 1938] which would be expected to show some level of separation. However because the wing is dynamically pitching, the stall point is expected to shift to higher angles of attack, later in the oscillation cycle resulting from the boundary layer enhancement effects noted by Ericsson and Reding [1988] and therefore the observation of flow attachment for this case is consistent.

At the outboard spanwise postions the wing tip vortex adds momentum to the flow on the suction surface and locally reattaches the flow near the tip. Specifically, the wing tip vortex forms from the re-balancing of the pressure gradient on the bottom (pressure) and top (suction) sides of the wing. This induces the motion of the air around the tip, from the pressure side to the suction side, while also entraining flow further away from the wing surface downward onto the suction side of the flexible wing a localized spanwise extent. This downard fluid motion helps to energize and stabilise the boundary layer near the wing tip maintaining attached flow at extremely high angles of attack (i.e. $\alpha = 30^o$).

In order to more clearly observe how this region of separation grows along the wing span, the location of separation is identified in the phase averaged SPIV images by finding the chordwise distance to the separation point. This procedure is applied to each of the three phase locations ($\phi = 204^o$, 214°, and 224°) and is presented in Figure 23. In the figure, the experimentally determined separation points are shown by asterisk data markers and a parabola was fit through each set (dashed lines) to highlight the separation distribution.

As the figure shows, the region of separation appears approximately parabolic in distribution. Furthermore, this region encompasses a localized area of the wing near the outer 2/3 span location. As the wing pitches through the phases, the parabolic region of separation grows in both spanwise and chordwise extent, however it remains localized. Specifically, while the lower bound of the separation region remains relatively fixed at $z/b = 0.58$, the upper boundary shifts to higher spanwise positions as the wing pitches to larger angles. This is because the wing tip reaches significantly higher angles of attack than the in-board regions of the wing. As the wing pitches up, the flow separation associated with these higher angles of attack become too significant for the influence of the tip vortex to overcome.

4.2   Rigid Wing Model

Utilizing the cyber-physical system approach discussed in Section 3.3, a comparison is made between the single frequency sinusoidally driven, which will be subsequently referred to simply as 'driven', and cyber-physical stall flutter, subsequently referred to as 'stall flutter',

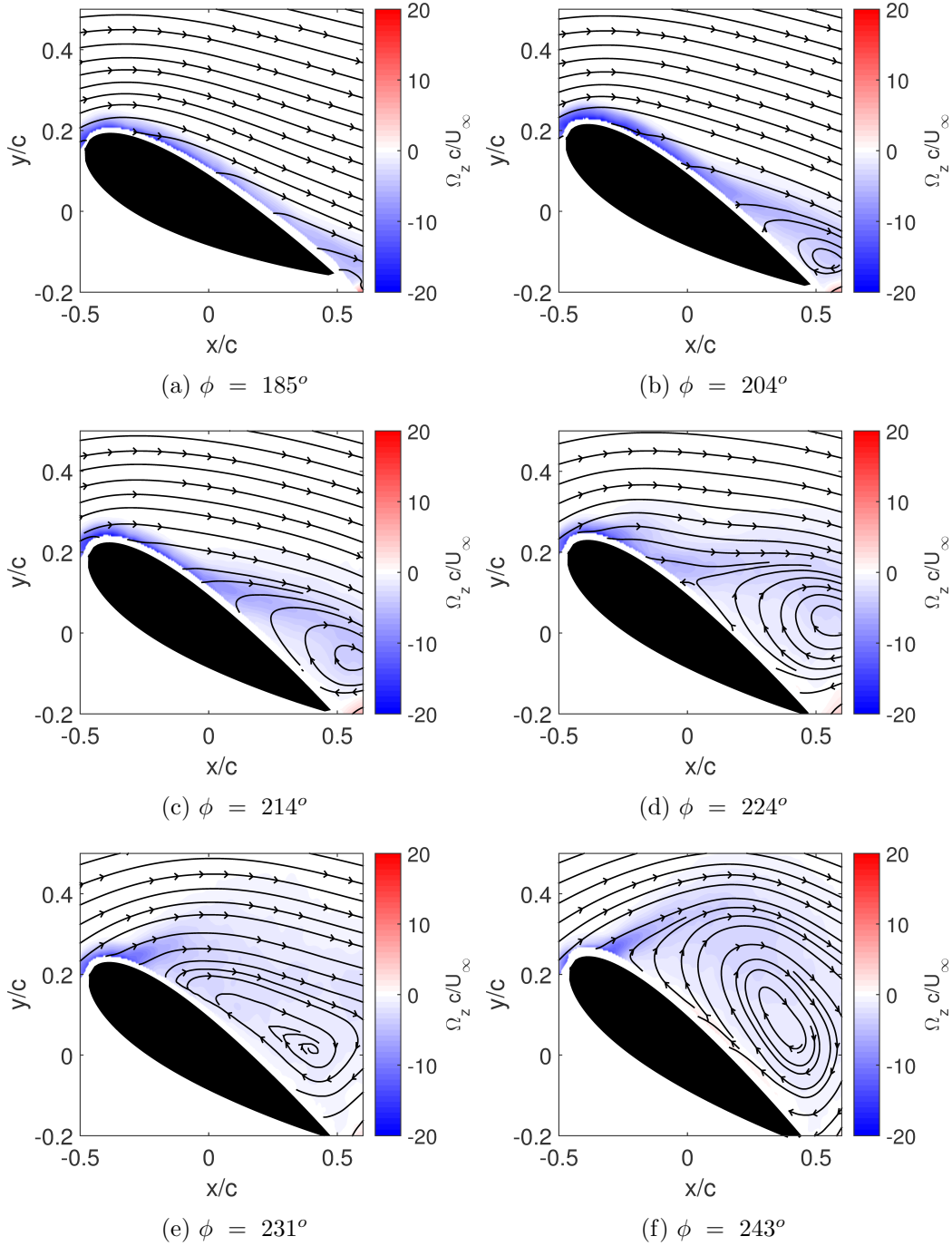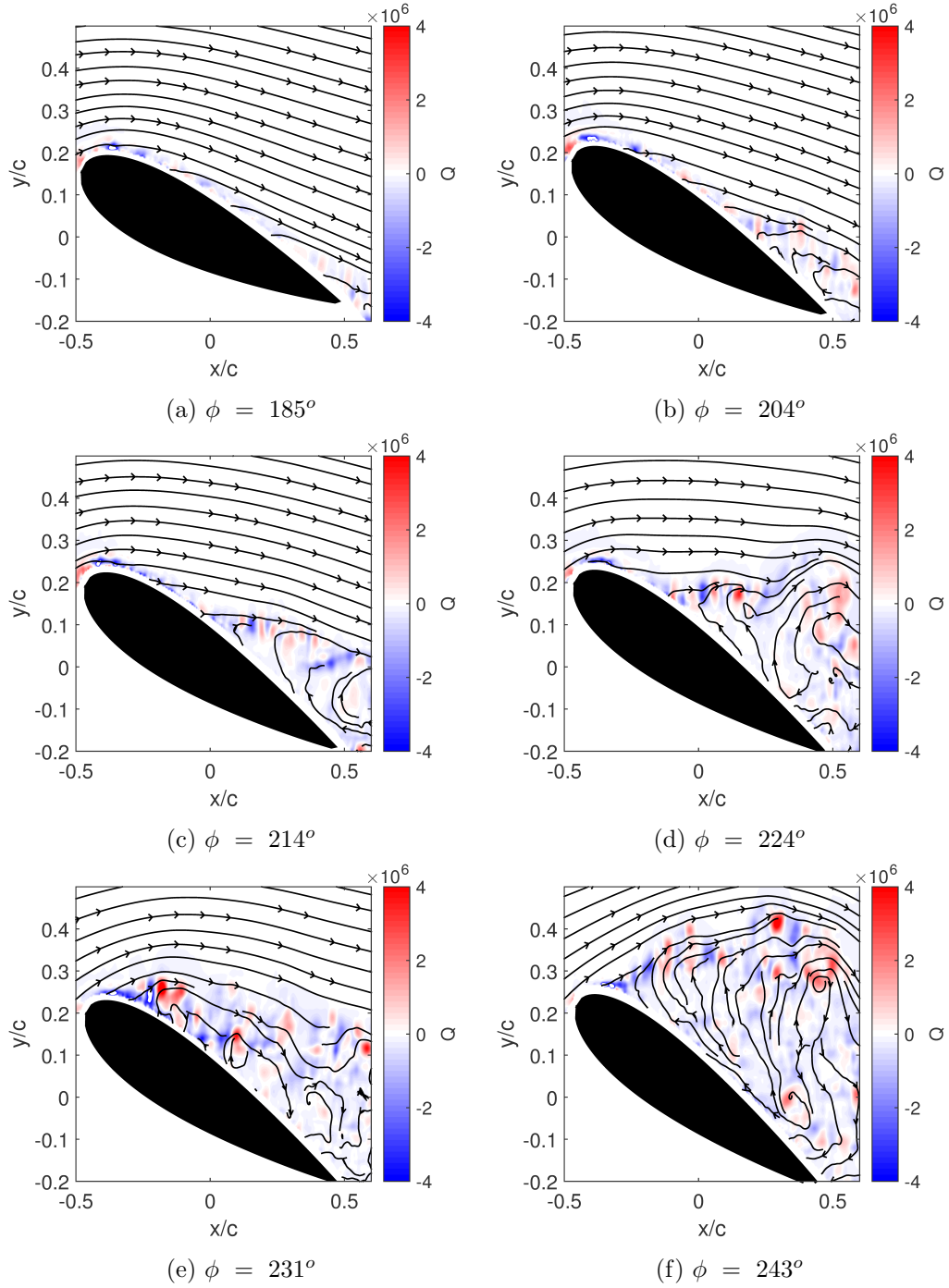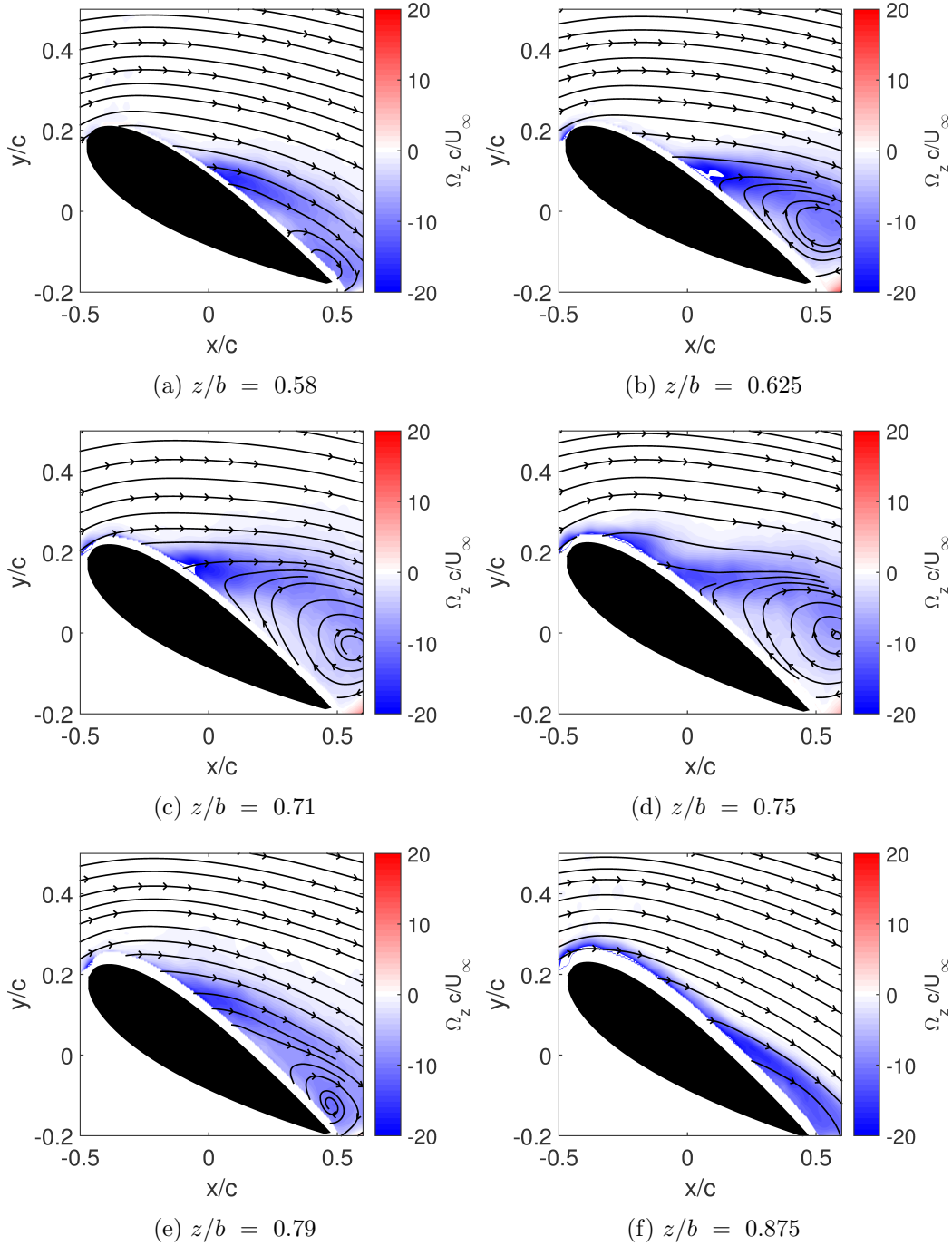Figure 22: Streamlines overlaid on contours of normalized vorticity from the phase-averaged flowfields around the flexible wing from $z/b = 0.58$ to $z/b = 0.875$ at a phase angle of $\phi = 224^o$.
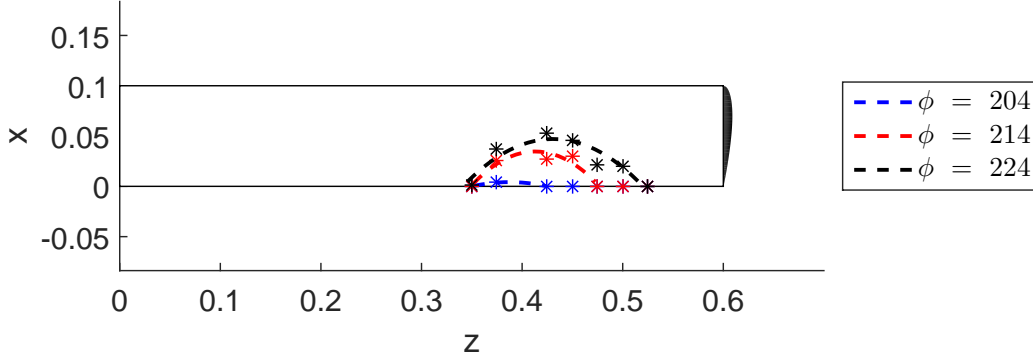
Figure 23: Spatial evolution of the region of flow separation along the span of the flexible wing model at the phase angles of $\phi = 204^o$, 214°, and 224° and span locations of $z/b = 0.58$, 0.625, 0.71, 0.75, 0.79, and 0.875. The dashed lines indicate the approximate location of $\overline{U} = 0$ from a parabolic fit through the experimental data points indicated by colored *.

operating modes for the NACA 0018 rigid wing. In order to approximately match system kinematics, cyber-physical, stall flutter cases were captured first. These cases were then post-processed and analyzed to determine the mean angle of attack, $\overline{\alpha}$, the pitch oscillation amplitude, A, and dominate frequency, ω, which were used to define the matching driven trajectory.

4.2.1   Pitching Moment Comparison - High Speed (USAFA)

From these comparisons, it was observed that the force production varied quite significantly between the driven and stall flutter modes of operation. These deviations were evident when comparing the moment coefficients about the rotation axis (50% chord) where, as discussed in Section 3.8, the moment coefficient is presented in two ways, namely as the aerodynamic pitching moment coefficient, C_m and the measured pitching moment coefficient $C_{m,Meas.}$. A comparison between a stall flutter and matched driven case is shown in Figure 24 for both C_m and $C_{m,Meas.}$ versus angle of attack, α. In this figure, the moment coefficient loops were traversed clockwise. For the stall flutter case, the cyber-physical system virtual parameters were tuned such that $k_\theta = 1.55 \frac{Nm}{rad}$ and $\eta_V = 0.015 \frac{Nm}{s\ rad}$. In both the stall flutter and driven modes of operation, the tunnel speed was set to $U_\infty = 26$ m/s.

It was observed that for this comparison case, there were significant differences between the moment response of the stall flutter and driven motions. This was true for both the aerodynamic pitching moment coefficient, C_m and the measured pitching moment coefficient $C_{m,Meas.}$. In the aerodynamic pitching moment coefficient, C_m, versus α plot, shown in Figure 24, it was observed that higher frequencies exist. These frequencies appeared to cause extra oscillations around the moment loop. For the C_m versus α loop of the driven motion, sharp changes in curvature occurred near the maximum and minimum angles of attack, however these sharp changes were not observed in the stall flutter case. That said it should be noted that the peak angular amplitudes between the two cases deviated significantly.

31

(a) C_m
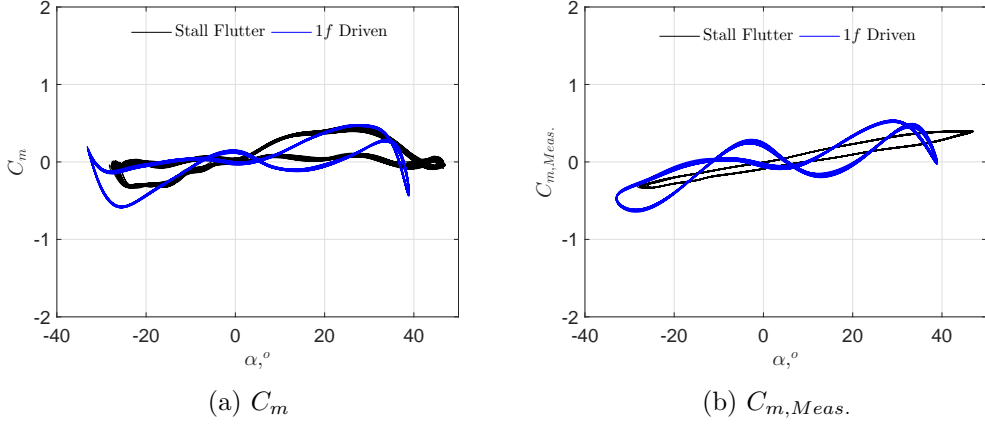
(b) $C_{m,Meas.}$

Figure 24: Comparison of C_m (a) and $C_{m,Meas.}$ (b) for the stall flutter and driven cases. Cyber-physical system of Fagley et al. [2016] utilized with $k_\theta = 1.55 \ \frac{Nm}{rad}$, $\eta_V = 0.015 \ \frac{Nm}{s \ rad}$, at $U_\infty = 26$ m/s.

(a) Stall Flutter

(b) $1f$ Driven
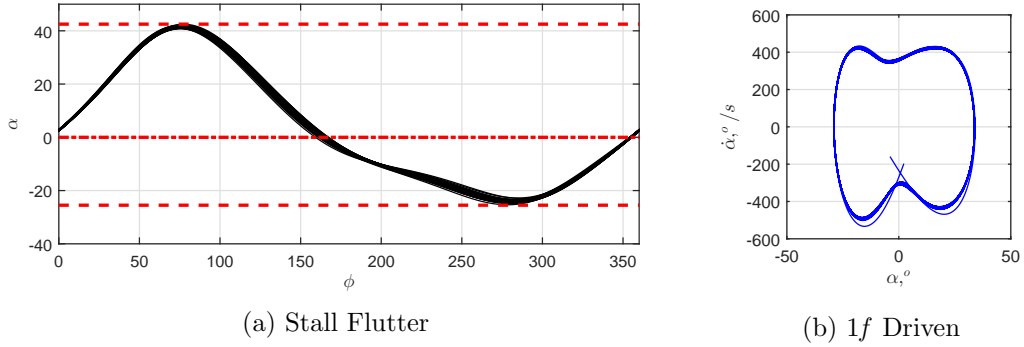
Figure 25: Sources of deviation between the prescribed driven motion and stall flutter kinematics: shifted $\overline{\alpha}$ (a) and non-sinusoidal driven motion as shown by phase plot (b).

This deviation was the result of two effects: 1) the matching procedure and 2) the control authority limitations of the system. These two contributions to the deviation between stall flutter and driven kinematics are visually explained in Figure 25. For the first effect, the driven motion was defined to match mean amplitude, time-averaged mean angle of attack, and mean frequency. In this instance, the stall flutter motion was not symmetric about its mean causing a bias between the time-averaged mean and the peak amplitudes as is shown in Figure 25a. The second effect was a result of the controller interplay with the fluid dynamics. Specifically, while the controller was prescribing a sinusoidal motion, non-linear aerodynamic forces were encountered. The time response of the controller and total motor torque then dictated how well the system could adapt to these forces without becoming non-sinusoidal. For the amplitudes and tunnel speeds in this case, this interplay caused the driven motion to deviate significantly from a pure sine wave as shown by the phase plot in Figure 25b. Note, a pure sine wave would produce a circular phase plot.

While there were several discrepancies in matching the driven and stall flutter cases presented in Figure 24, some physical insight can still be gained. Specifically, because

the driven motion did not allow the wing to move with respect to the externally applied aerodynamic torque, there was a decoupling of the wing position and the aerodynamics. This can be examined by looking at the force response near $\alpha = 30^o$ in Figure 24a. In this region the stall flutter and driven trajectory moment coefficients overlap. Traversing the two moment coefficient loops along the pitch-up, or clockwise, direction, the stall flutter trajectory continued to higher angles of attack, however the driven motion was abruptly forced to decreasing angles of attack. The continuation of the stall flutter motion to higher angles of attack indicated that the aerodynamics were likely continuing to apply a large force. In contrast, the driven kinematics moved to a lower angle of attack thereby producing a significant differential between the applied motor torque and the aerodynamic moment leading to abrupt changes in moment loop curvature.

When analyzing $C_{m,Meas.}$ presented in Figure 24b, the character of the pitching moment changed, significantly. Specifically, while the aerodynamic pitching moment coefficient, C_m showed higher frequency oscillation, the measured moment coefficient $C_{m,Meas.}$ collapsed to a relatively simple elliptical response. This collapse demonstrated that the structure introduced a stabilizing effect to the system. This effect was not observed in the driven case, however it should be noted that since the driven kinematics differed from stall flutter, direct comparisons are potentially misleading.

4.2.2   Pitching Moment Comparison - Low Speed (UCB)

Due to the aforementioned issues of control at the higher tunnel speeds, the wind speed was reduced and tests were repeated using the cyber-physical system and wind tunnel facilities at the University of Colorado Boulder. In the following discussion, a low speed case is analyzed which exhibited highly sinusoidal stall flutter thereby ensuring as equivalent of a comparison as possible to the driven motion. The kinematics of the stall flutter and driven motion for this low speed case is summarized in Figure 26, where the resulting moment coefficients, both C_m and $C_{m,Meas.}$ are shown in Figures 26d and 26e. Note that the plots in Figures 26b, 26c, 26d, and 26e show phase averaged trajectories. For this stall flutter case, the cyber-physical system was tuned such that $k_\theta = 1.54$ N m/(rad), $\eta_v = 0.013$ N m/(s rad), and $U_\infty = 15.2$ m/s.

In Figure 26a the frequency spectra of the angular position shows a dominant peak at 3.2 Hz, with the $2^{nd} - 4^{th}$ harmonics also visible. These frequency peaks are observed in both the stall flutter (black) and driven (blue) motions, however the stall flutter case displays broader higher harmonic peaks, as compared with the driven motion. This potentially indicates that the stall flutter motion retains more energy at these higher frequencies, though the 3.2 Hz peak is still dominant. From these frequency spectra it is expected that both motions are nearly sinusoidal. This is verified by overlaying a single sine wave on the mean trajectories of both the driven and stall flutter motions in Figure 26b. This overlay shows that the driven motion almost exactly follows the sine wave, with some small deviations. The stall flutter motion is also close to a sine wave, though larger deviations persist near the peak amplitude locations.

While the trajectory of the angle of attack appears largely sinusoidal, higher (harmonic) frequencies are present as indicated by the frequency spectra. These higher frequencies are important when analyzing the acceleration profiles, which are shown in Figure 26c for both the driven and stall flutter motions. Specifically, the higher harmonics cause the accelera-

tion profiles to deviate significantly away from a simple sinusoidal profile. From a purely mathematical perspective this makes sense as the small, periodic deviations from the sinusoidal position trajectory (see Figure 26b) will be contained in the higher harmonics of the spectra. The influence of these higher frequencies is then amplified through the double differentiation of the position trajectory to arrive at the acceleration profile. Because force is proportional to acceleration, these frequencies demonstrate the effects of the nonlinear aerodynamic behavior for the dynamically pitching wing, and how it can significantly influence driven or prescribed motions. This further implies that even small deviations from the prescribed sinusoidal trajectory can have a strong influence on the the aerodynamic force production. This also demonstrates the difficulty in performing precise pitching wing or dynamic stall experiments, because if one is not careful they can create significantly different force trajectories from similarly prescribed motions.

From the moment loop comparisons in Figure 26d it is evident that while the stall flutter and driven signals show similar behavior, the driven motion exhibits slightly larger pitching moments with differing post-stall behavior. To quantify this difference, a root mean square difference can be calculated between the two, phase averaged pitching moment signals using Equation (10) where $C_{m,F}$ refers to the flutter pitching moment and $C_{m,D}$ refers to the driven. This RMS difference effectively provides a standard deviation of the differences between each pitching moment versus phase signal. This equation can then be similarly written for $C_{m,Meas.}$. Performing this calculation, the root mean square difference between the stall flutter and driven cases was found to be 0.19 for C_m, and 0.20 for $C_{m,Meas.}$. In terms of pitching moment coefficient, a deviation of approximately 0.2 is quite significant.

$$RMS = \sqrt{\frac{1}{N} \sum_{\phi\,=\,0}^{N} \left(C_{m,F}(\phi) \,-\, C_{m,D}(\phi) \right)^2} \tag{10}$$

4.2.3   Planar PIV - Low Speed (UCB)

To further understand the deviations in the aerodynamic force production between the driven and stall flutter motions, planar PIV measurements are presented, focusing at cycle locations near the positive maxima in C_m and $C_{m,Meas.}$. In total six phase angles are examined at $\phi = 220^o$, 232°, 244°, 273°, 297°, and 309°. Figure 27 shows where these phases are aligned in the cycle in terms of both kinematic and aerodynamic moment profiles. This figure presents the phase-averaged: aerodynamic pitching moment coefficient, C_m, measured pitching moment coefficient, $C_{m,Meas.}$, and α versus phase angle for both the stall flutter and driven motions. The dashed red vertical lines correspond to each of the phase locations where the PIV measurements discussed here were collected. As the figure shows, the first four phases captured pitch-up kinematics while the final two phases captured the post-stall, pitch down kinematics. Specifically, $\phi = 220^o$ corresponds to approximately $\Delta\phi \approx +6^o$ after the C_m peak and $\Delta\phi \approx -6^o$ before the $C_{m,Meas.}$ peak in the driven cycle where this spacing is the result of the phase resolution of the collected PIV data. $\phi = 232^o$ corresponds to an intersection of the C_m curves for driven and stall flutter motions and the approximate peak in $C_{m,Meas.}$ for the stall flutter motion. $\phi = 244^o$ corresponds to an increasing deviation in C_m between the stall flutter and driven motions and $\Delta\phi \approx +12^o$ after the peak stall flutter C_m. $\phi = 273^o$ captures a local minima in C_m and $C_{m,Meas.}$. Finally, $\phi = 297^o$ and 309°

(a) Frequency Spectrum

(b) α versus ϕ

(c) $\ddot{\alpha}$ versus ϕ

(d) C_m
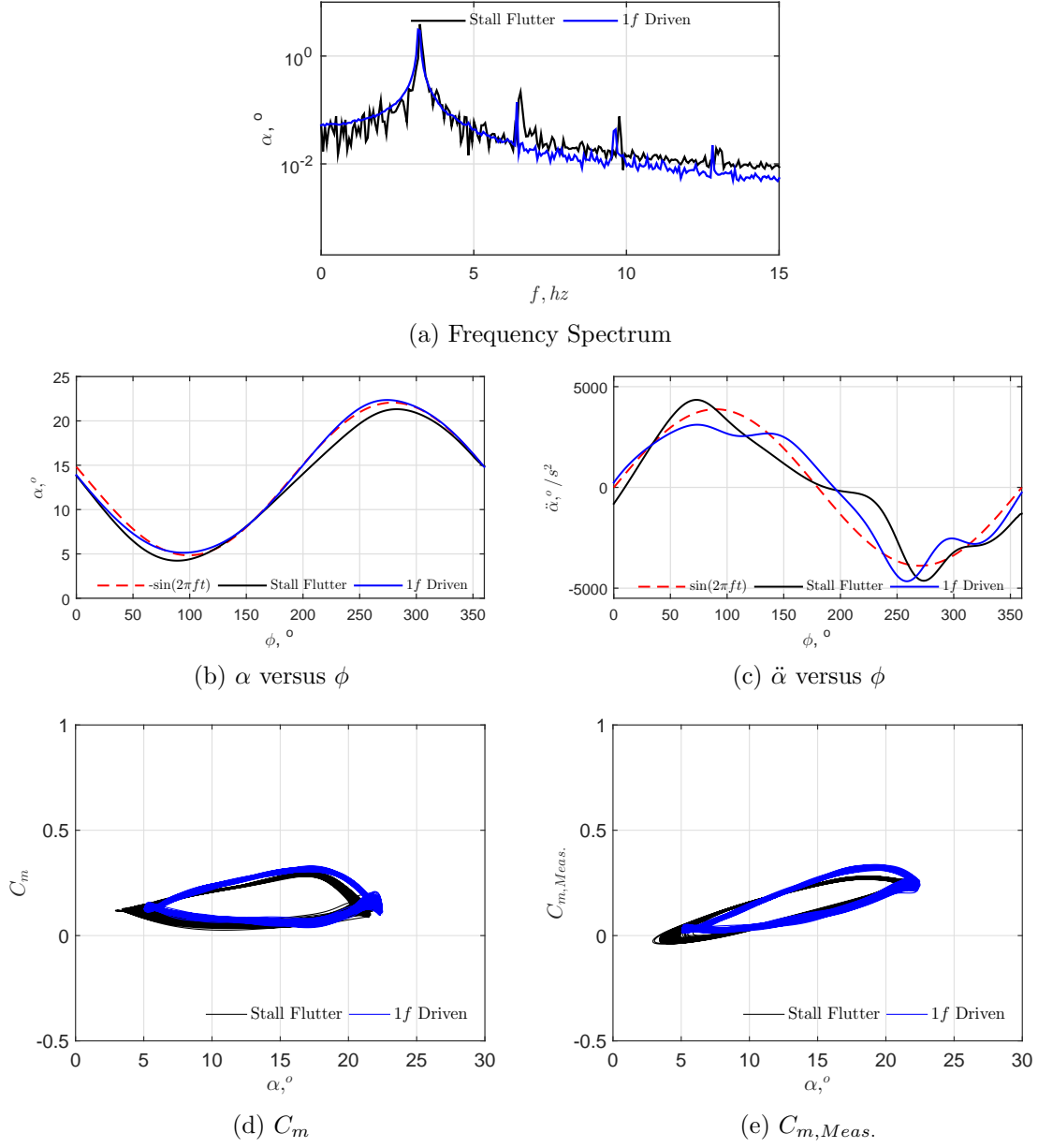
(e) $C_{m,Meas.}$

Figure 26: Comparisons of frequency spectrum (a), phase averaged angle of attack (b), phase averaged angular acceleration (c) versus ϕ, and C_m (d) and $C_{m,Meas.}$ (e) versus angle of attack signals for matched low speed stall flutter and driven cases.

(a) C_m

(b) $C_{m,Meas.}$

(c) Angle of Attack, α
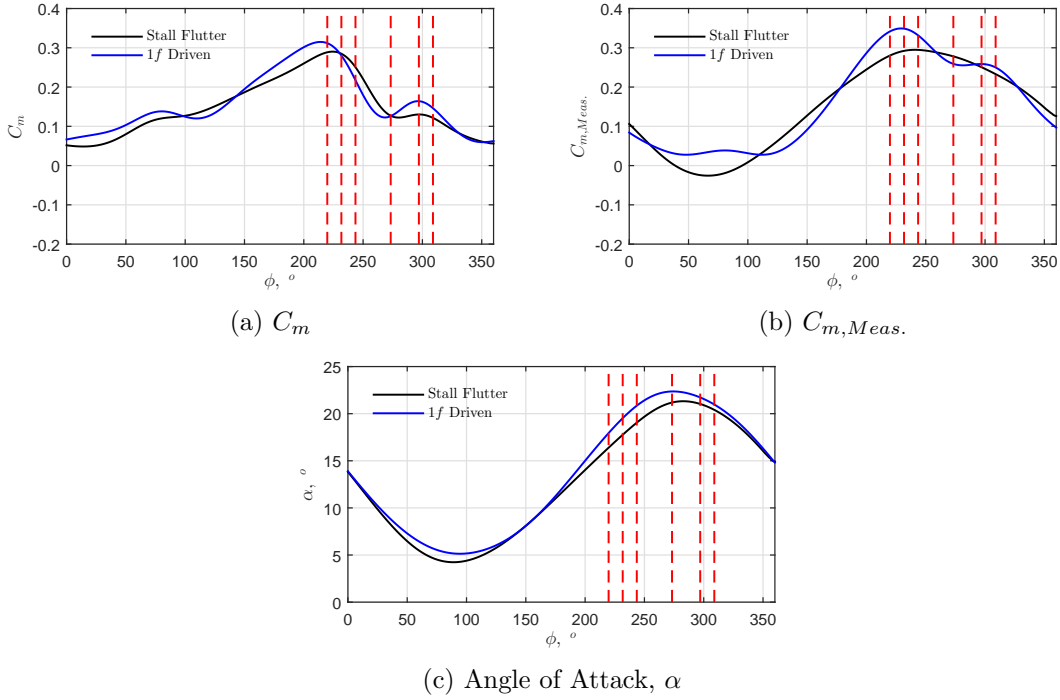
Figure 27: Plots of phase averaged: C_m (a), $C_{m,Meas.}$ (b), and α (c) versus phase angle with overlays of the six presented PIV measurement phase angles, $\phi = 220^o$, 232°, 244°, 273°, 297°, and 309°.

correspond to the formation and shedding of a secondary leading edge vortex (LEV). The resulting flow fields for each of these phase locations are shown in Figure 28 and 29 for the driven and stall flutter cases respectively. In these figures streamlines are plotted with color contours of the normalized spanwise vorticity, $(\Omega_z\ c)/U_\infty$.

The differences in pitching moment near the the first maximum, as shown in Figures 26d and 27 are potentially explained from the PIV measurements at $\phi = 220^o$ and 232°, which show that LEV formation occurs earlier in the driven motion as compared to stall flutter. Specifically, as is shown in Figs. 28a and 29a, a vortex begins to roll up around the leading edge as the wing pitches up. By $\phi = 232^o$ a coherent LEV has formed for the driven motion, as is shown in Figure 28b. In contrast, while the stall flutter motion does show a vortex appearing at $\phi = 232^o$ the vortex does not appear to be as strong or as coherent through $\phi = 244^o$ as shown in Figure 29c.

As Figure 27 shows, the aerodynamic pitching moment, C_m, drops significantly after the first maximum. This is likely the result of the dynamic stall vortex advecting further down the chord of the wing, which reduces the moment arm between the low-pressure imposed by the vortex core on the wing surface and the rotation axis. This finding agrees with arguments made by Onoue and Breuer Onoue and Breuer [2016] for a pitching flat plate and is supported by Figure 28c showing that while the LEV grows in size, its centroid moves closer to the rotation axis.

By $\phi = 273^o$, both the stall flutter and driven cases pass their respective maximum pitching moments. In the driven case, a trailing edge vortex appears to have shed from the

36

airfoil, as is indicated by the region of positive vorticty, and a second LEV begins to form. In the case of stall flutter (Figure 29d), the trailing edge vortex is still present, however a coherent second LEV has yet to fully form.

Following the initial LEV vortex shedding cycles, a second LEV forms and sheds during both the driven and stall flutter cycles. This second LEV is clearly visible at $\phi = 297$ and 309, given in Figs. 28e and 28f for the driven motion, and Figs. 29e and 29f for the stall flutter motion. This secondary shedding cycle is responsible for producing an inflection in the C_m and $C_{m,Meas.}$ versus ϕ trajectories that creates the second local maxima in Figs. 27a and 27b. Furthermore, this inflection explains why the small loop near maximum α is observed in Figure 26d. Specifically, while angle of attack is beginning to decrease, C_m momentarily changes direction of curvature and increases. A similar inflection, but paired with a smaller peak is observed in the stall flutter trajectory. This is consistent with the smaller amplitude change in C_m as well as the more gradual change in angle of attack shown in Figure 27c. It should be noted that this second shedding cycle is slightly different than the first. Specifically, while the first LEV cycle showed significant variation between the driven and stall flutter motions, in the second cycle the vortex size and phase development are quite similar. Specifically, the driven motion does not appear to lead in the formation of this second LEV, but instead both Figs. 28e and 29e show similarly sized vortices with comparable vorticity, encompassing the full chord of the airfoil. Additionally by $\phi = 309^o$ both the driven and stall flutter motions have shed their respective LEVs leaving behind a second TEV. The stall flutter case does appear to show a slightly smaller second TEV, as compared with the driven case, however as was demonstrated in Figure 27 at these phase locations, the two motions show similar pitching moment magnitudes.

4.2.4   Circulation Comparison - Low Speed (UCB)

To more quantitatively analyze the strengths of the vortices in the flow, the circulation above the airfoil surface was calculated through an integration of vorticity as provided by Equation (11).

$$\hat{\Gamma}_z = \frac{1}{cU_\infty} \int_A \Omega_z dA \tag{11}$$

A sample integration region is shown in Figure 30, where the dashed red lines show the region's boundaries. This approach was used to provide a semi-quanitative comparison between the driven and stall flutter cases. Using this approach, the circulation was obtained for the presented phases and provided in the table shown in Table 3. As the table shows, for the initial LEV formation captured from $220^o < \phi < 244^o$, the driven motion creates significantly more circulation. This result agrees with the qualitative arguments presented previously and the flow fields shown in Figs. 28 and 29. Furthermore, this result makes sense from a conservation of circulation perspective. Specifically, through the first shedding cycle, the driven wing reaches higher angles of attack sooner in phase than the driven. From this behavior, it would be expected that a larger starting vortex would form, containing greater circulation in the driven motion, than in the stall flutter motion. In the second shedding cycle the calculation shows that circulation magnitudes are much more comparable, though the driven motion still reaches a higher maxima. This finding is again consistent with previous observations.

Due to the larger circulation in the driven cycle, it was expected that the driven motion

(a) $\phi = 220$, $1f$ Driven

(b) $\phi = 232$, $1f$ Driven

(c) $\phi = 244$, $1f$ Driven

(d) $\phi = 273$, $1f$ Driven

(e) $\phi = 297$, $1f$ Driven

(f) $\phi = 309$, $1f$ Driven
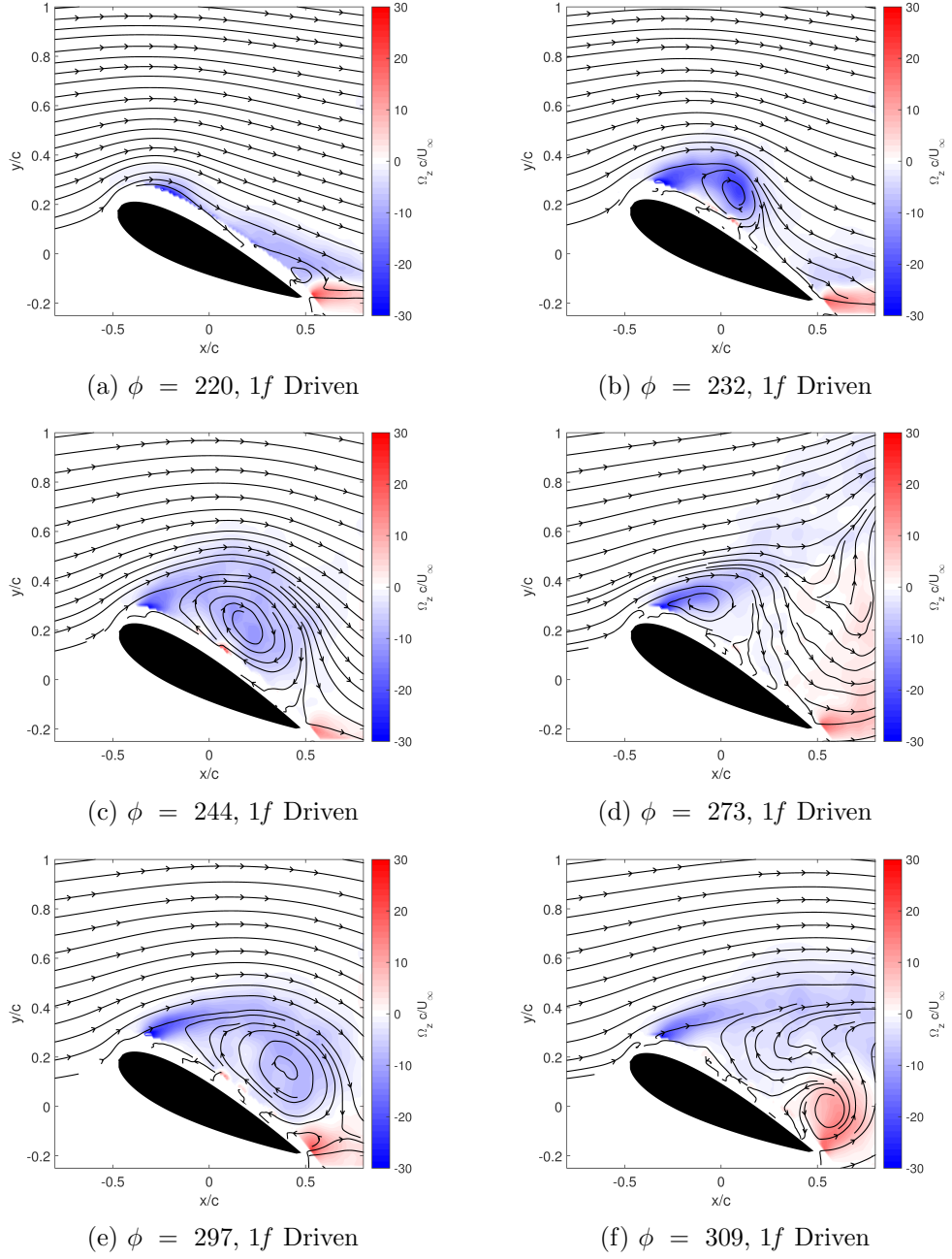
Figure 28: Streamlines and contours of vorticity, Ω_Z, at select phases for the driven motion.

(a) $\phi = 220$, Stall Flutter

(b) $\phi = 232$, Stall Flutter

(c) $\phi = 244$, Stall Flutter

(d) $\phi = 273$, Stall Flutter

(e) $\phi = 297$, Stall Flutter
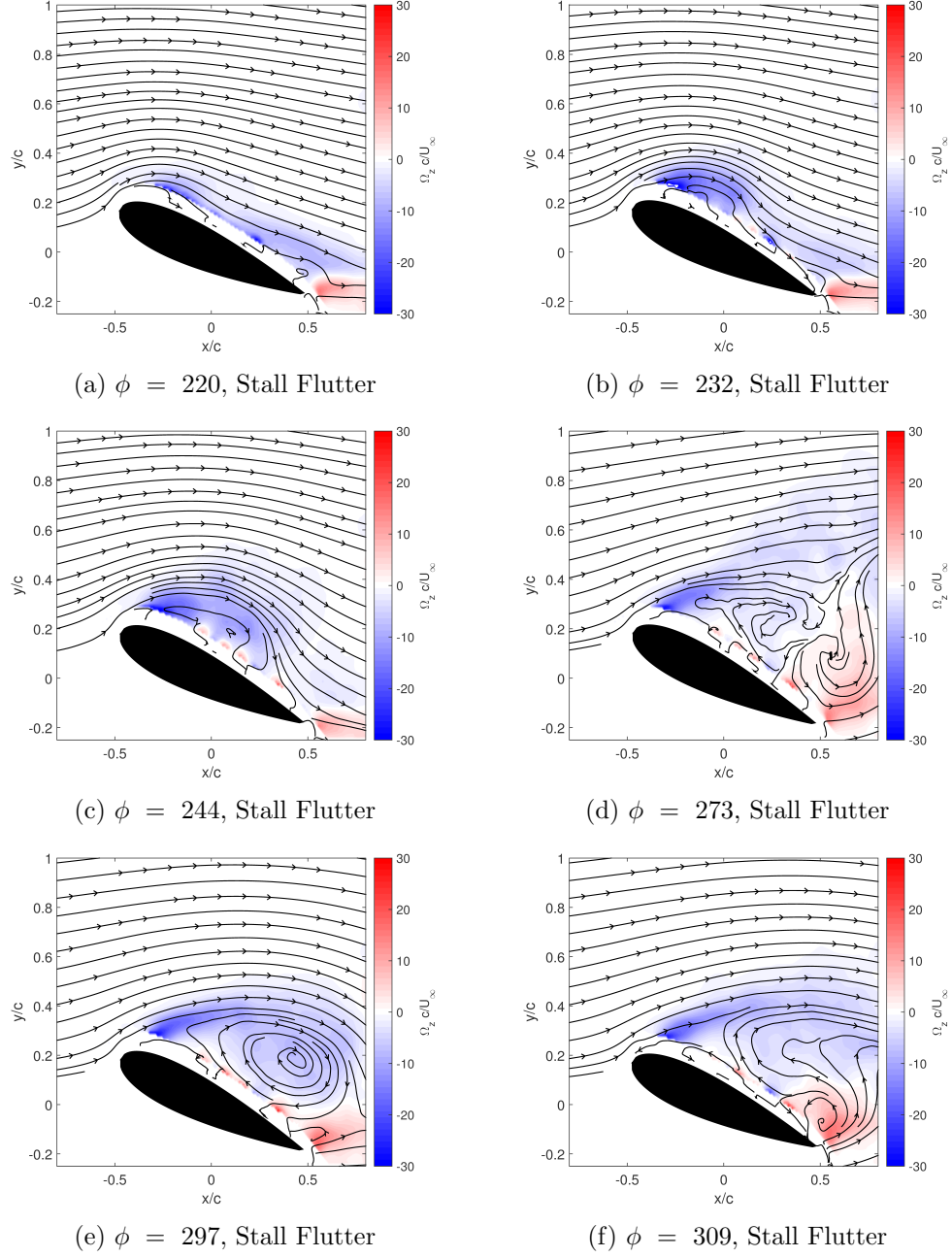
(f) $\phi = 309$, Stall Flutter

Figure 29: Streamlines and contours of vorticity, Ω_Z, at select phases for the stall flutter motion.

Table 3: Calculated circulation, $\Gamma(10^2)$, for select phases.

ϕ	**StallFlutter**	**$1f$ Driven**
220	-10.0	-16.1
232	-97.4	-63.3
244	-153.5	-92.5
273	-54.3	-61.3
297	-126.2	-93.8
309	-72.8	-70.9
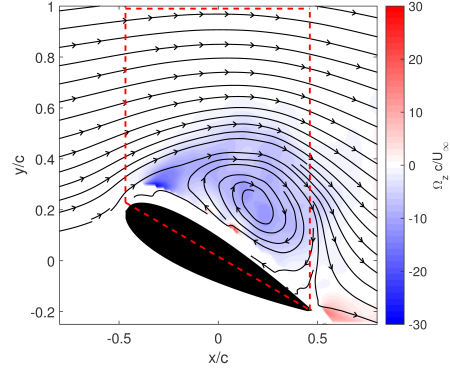
Figure 30: Boundary for circulation calculation.
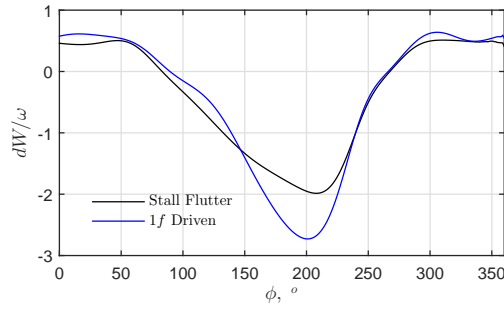
Figure 31: Comparison of aerodynamic differential work dW normalized by cycle frequency, ω, for driven and stall flutter cases.

operated in a higher energy state than the stall flutter motion. Since the two kinematic trajectories were similar, it was also expected that this higher energy state was associated with a less stable flowfield. In order to demonstrate this, the aerodynamic differential work:

$$dW \equiv -C_m d\alpha, \tag{12}$$

was calculated as discussed by McCroskey McCroskey [1981]. With this definition, negative dW implies the fluid is doing work on the wing and the wing will tend towards instability, while positive dW implies the wing is doing work on the fluid and will tend towards stability McCroskey [1981]. The result of this calculation is shown in Figure 31. This figure shows that the negative dW in the driven case peaks at an amplitude 27% higher than in the stall flutter case. This demonstrates that the driven motion is producing a less stable flowfield, which is consistent with the increased circulation and faster shedding noted previously. The dW cycle also shows that during the pitch up portion of the motion, from $\phi \approx 85^o$ until $\phi \approx 270^o$ the aerodynamic damping is negative. This makes sense as it implies the aerodynamic forces are dominating the structural restoring forces causing the wing to pitch up. During the remaining phases, the wing is pitching down implying that the structural restoring forces are dominating the aerodynamic and the wing is doing work on the structure. This is verified by the positive value of dW.

5   Conclusions

As part of this sponsored research effort the PI and GRA conducted experimental research focusing on elucidating the baseline kinematics and aerodynamics associated with stall flutter in both flexible and rigid wing models. In both cases, a position-feedback cyber-physical (electro-mechanical) system was utilized to simulate the structural mechanics of the wing models. This cyber-physical system allowed for an in situ tuning of the wing's structural properties through manipulating the gains in the second-order motor control system. Additionally, the cyber-physical system was designed to directly control only one degree-of-freedom, namely the wing pitch axis (i.e. rotational axis aligned parallel to the span). In the flexible wing, this allowed for dynamic variations in the wing twist distribution through the prescription of the wing tip twist angle by the cyber-physical system; as the wing root was maintained at a geometrically fixed angle of attack. For the rigid wing, the entire wing span was allowed to rotate. Thus the cyber-physical system prescribed a uniform pitch angle (or angle of attack) for the entire wing (i.e. rigid body rotation).

Flexible Wing Experiments   The flexible wing model consisted of a finite-span, rectangular wing section with a semi-span aspect ratio of six and composed of a NACA 0018 profile. For the flexible wing study, the model's torsional stiffness, damping and inertia were maintained at $k_\theta = 0.47~N~m~rad^{-1}$, $\eta = 6.09 \times 10^{-3}~N~m~s~rad^{-1}$, and $J = 4.25 \times 10^{-4}~kg~m^2~rad^{-1}$, respectively, while the wind tunnel was regulated to a constant free-stream velocity of $U_\infty = 26~m/s$. At these conditions a torsion dominated limit-cycle oscillation was observed and was thoroughly classified as a stall flutter phenomena through detailed measurements of the wing kinematics.

The flexible wing's kinematic motion was experimentally measured through the use of a stereo-vision motion capture system. The surface motion was then decomposed into the

principle components of torsion and bending, which through a modal analysis were projected onto the first three-classical modes for a clamped-free beam in either torsion or bending vibration. From the modal analysis of the wing kinematics, it is apparent that the model deforms primarily in torsion and that this deformation is principally composed of the first mode of torsional vibration with small amplitude contributions from higher order modes. Furthermore, the motion was shown to oscillate at two frequencies, which qualitatively correlated to the torsional and bending natural frequencies of the model ($\omega_\theta = 5.66\ Hz$ and $\omega_h = 11.45\ Hz$). From the eigenmode analysis a two equation empirically fitted model of the wing kinematics was then developed, and showed very good agreement with the raw stall flutter data. The stereo-vision results corroborated the wing-tip angular displacement measurements made with the optical encoder in the cyber-physical system, thus validating this approach for experimentally replicating and monitoring stall flutter on the test article. While the empirical model did a good job of capturing the mean motion observed, its predictive capability is limited by the independently fitted weights for each eigenmode included within the model. Furthermore, additional work would be required to better model the time dependent variation in frequency and phase, as well as the beat observed in the bending signal across the full testing period.

In addition, to the kinematic measurements aerodynamic moment and flowfield measurements were also made on the flexible wing model. The internal pitching moment was computed based upon the internal moments in the flexible wing model and the torque applied by the cyber-physical system. This calculation demonstrated that the maximum pitching moment observed by the cyber-physical system occurred well before the peak angle of attack of approximately $\alpha = 30^o$. The peak pitching moment appeared to occur just before flow separation was initiated at the wing trailing edge and well before it had fully developed. From the pitching moment, differential work was calculated showing that the majority of the pitching cycle was defined by negative dW which corresponded to negative damping and a tendency to grow in amplitude. At the turning locations dW became slightly positive indicating a re-stabilization of the wing system which bounds the growth of the stall flutter LCO and may have been associated with massive flow separation at the maximum angle of attack and reattachment at the minimum angle of attack. Finally, it should be noted that since the C_m presented did not incorporate forces at the second boundary (i.e. the wing root), this measure could only provide a partial representation of the fluidic forces.

To understand the initial growth of separation on the flexible wing surface, stereoscopic particle image velocimetry was collected at different phase angles in the oscillation cycle and spanwise locations along the wing. From the phase sweep data it was found that the growth of separation on the flexible wing was largely defined by the trailing edge initiated separation of the shear layer rather than the formation of a leading edge vortex as is typically observed in rigid body dynamic stall. This separation event produced small structures within the shear layer that were not coupled or locked to the primary oscillation frequency of the wing. From the spanwise SPIV data it was found that the separation was initiated from a small parabolic region which grew from the trailing edge in chordwise and spanwise extent at as the local angle of attack increased. That said the flow separation remained largely restricted to the outer 2/3 span region on the flexible wing. Finally, even with no data beyond the maximum angle of attack or during pitch down motion, the authors strongly believe that the data shows that no large-scale, coherent dynamic stall vortex was formed by the flexible wing during stall flutter.

Rigid Wing Experiments The second phase of the research effort focused on understanding the kinematic and aerodynamic differences between stall flutter and a prescribed sinusoidal pitching (driven) motion on a rigid wing section. Tests using the identical wing system were carried out in wind tunnels at both USAFA and UCB. It was found that even when the kinematics were more closely matched at lower freestream velocities, $U_\infty = 15.1$ m/s, there were still noticeable differences in the pitching moments for the driven and stall flutter cases. It is argued that these differences are related to higher frequencies present in the cycle trajectories. Specifically, while these frequencies appeared small in the α trajectory, they are significant in the acceleration profile due to magnification from differentiation. Furthermore, from Newton's law ($F = m\,a$), it is well understood that these deviations in acceleration imply significant changes in aerodynamic force production and subsequently the aerodynamic pitching moment applied.

In order to understand how the flowfield was related to these differences in pitching moment, planar PIV data was collected near the point of maximum pitching moment in the cycle. From the PIV results it was found that these differences could be attributed to the formation and subsequent shedding of a leading edge vortex in both the driven and stall flutter cycles. For both motions, two vortex shedding events occurred, one near the maximum pitching moment coefficient and a second at a later phase angle near another local maxima in the pitching moment coefficient. For the driven case, the initial leading edge vortex developed faster and grew larger than in the stall flutter case; attaining a maximum circulation approximately 1.6 times the magnitude of the maximum for the stall flutter case. This was argued to be the result of the driven wing having a faster pitch-up rate, $\dot{\alpha}$ as compared to the stall flutter case. In order to conserve circulation in the field, this then required the formation of a larger vortex. Interestingly, the secondary formation and shedding cycle occurred at similar phases for both the driven and stall flutter motions even though the primary shedding events occurred at different phases. Throughout the cycle, both motions produced similar pitching moments and amounts of circulation across the suction surface of the wing, though the results for the driven motion were measurably larger than for stall flutter.

Finally, the differential work, dW, was calculated to provide a measure of aerodynamic damping on the rigid wing model. This calculation was argued to show that the driven motion produced a less stable flowfield than the stall flutter motion due to a 27% increase in peak negative dW. It was further shown that during the pitch-up portion of the cycle, the aerodynamic forces dominated the structural forces as indicated by negative dW. Inversely, and as expected, the structural restoring forces dominated the aerodynamic forces during pitch-down portion of the cycle.

6   Recommendations for Future Work

While the current research effort made significant progress towards understanding the fundamental kinematics and flow physics associated with stall flutter on both flexible and rigid wing sections there is still significantly more that can be done. The first major recommendation for future work is to better understand the influence that flow control has on both the flowfield and the structural response of a wing in a stall flutter limit cycle oscillation. The collaborators of the PI and GRA at USAFA have already made significant progress towards studying the influence of flow control both through computational simulations and

experimental studies. Their results have showed great promise, but they have been limited to using only a single steady-blowing jet; which required an air supply and a solinoid valve in the experiments. The PI believes that future work utilizing an array of zero-net-mass flux devices, such as synthetic jet actuators, has the potential to further improve the ability of flow control to attenuate stall flutter on the flexible wing.

In addition to the change in actuation type, another challenge associated with the current studies is that the stall flutter motion and impact of flow control are being studied only after a stall flutter LCO has stabilized. To actually mitigate the impact of stall flutter in real systems it needs to be attenuated before the oscillations grow into stable LCOs. As a result, the transient growth of the LCO needs to be studied under deterministic and physically relevant conditions. As a result developing a method of physically perturbing the wing system to deterministic ally grow into an LCO would be highly desirable. Once this is devised and demonstrated then the transient behavior can be studied and novel flow control strategies could be devised.

Finally, from the rigid wing work it was found, not surprisingly, that the pitch-up speed and acceleration critically influence the force production and leading edge vortex development. Furthermore, a wing undergoing stall flutter was observed to have a much slower pitch-up rate as compared to a wing driven in a sinusoidal fashion at a similar primary frequency. This suggests that future work needs to be carried out to understand how the force production (and flow structures) change as the waveform shape is skewed for a fixed periodic frequency.

7 Accomplishments

Multiple accomplishments were achieved throughout the course of this research program. The scientific and technical findings of the program were discussed in detail above. The current section serves to summarize the various accomplishments, such as: honors and awards received, presentations given, and manuscripts that were (or will be) published as a result of this work.

7.1 Honors and Awards

At the beginning of the the performance period the GRA, Ethan Culler, working with the PI applied for and was selected to receive a National Defense Science and Engineering Graduate (NDSEG) Fellowship. The fellowship is sponsored by the Air Force Office of Scientific Research (AFOSR) and was announced to the GRA on April 14, 2015. This fellowship covered the GRAs stipend (salary) and tuition starting on September 01, 2015 and continuing for three calendar years to August 31, 2018. As a result the cooperative agreement budget was modified to reallocate the GRA summer salary funds towards travel expenses, materials and supplies for the project to enhance the research funded under this cooperative agreement. This budget modification was subsequently approved by the contracting office at USAFA on August 27, 2015. Finally, the later conclusion of the GRAs fellowship (relative to the performance period of the current cooperative agreement) will allow for the continuation of the research and completion of the technical works labeled as "Forthcoming" below.

7.2   Publications and Presentations

A brief listing of all of the presentations and publications that resulted from this work is provided below:

Presentations

1. **J. Farnsworth**. Towards Controlling Stall Flutter on Flexible Finite Span Wings. Invited Seminar. *University of Maryland*, College Park, MD, July 20, 2015.

2. **E. Culler and J. Farnsworth**. Spanwise Variation of Stall Flutter on a Flexible NACA 0018 Finite Span Wing. Oral Presentation. Rocky Mountain Fluid Mechanics Research Symposium 2015, Boulder, CO, August 4, 2015.

3. **E. Culler, J. Farnsworth**, C. Fagley, and J. Seidel. Spanwise Variation of Stall Flutter on a Flexible NACA 0018 Finite Span Wing. Oral Presentation. AIAA Rocky Mountain Section 2015 Annual Technical Symposium, Golden, CO, November 6, 2015.

4. **E. Culler, J. Farnsworth**, C. Fagley, and T. McLaughlin. Spanwise Variation of Stall Flutter on a Flexible NACA 0018 Finite Span Wing. Oral Presenation. 54th AIAA Aerospace Sciences Meeting, AIAA SciTech Forum, San Diego, CA, January 4-8, 2016.

5. **E. Culler, J. Farnsworth**, C. Fagley, and J. Seidel. Comparison of driven and simulated "free" stall flutter in a wind tunnel. Oral Presentation. 69th Annual Meeting of the American Physical Society's Division of Fluid Dynamics, Portland, OR, November 20-22, 2016.

6. **E. Culler, J. Farnsworth**, C. Fagley, and T. McLaughlin. Driven versus "Free Flutter" Motion of a NACA 0018 Finite Span Rigid Wing. Oral Presenation. 35th AIAA Applied Aerodynamics Conference, AIAA AVIATION Forum, Denver, CO, June 5-9, 2017.

7. **E. Culler, J. Farnsworth**, C. Fagley, and J. Seidel. The Influence of Second Harmonic Phase and Amplitude Variation in Cyclically Pitching Wings. Oral Presentation. 70th Annual Meeting of the American Physical Society's Division of Fluid Dynamics, Denver, CO, November 19-21, 2017 (Forthcoming).

Conference Proceedings

1. C. Fagley, J. Seidel, and T. McLaughlin, and **J. Farnsworth**. Aero-Servo-Elastic Control of a Cyber-Physical Flexible Wing. In *AIAA Paper 2016-0320*, January 2016.

2. **E. Culler, J. Farnsworth**, C. Fagley, and T. McLaughlin. Spanwise Variation of Stall Flutter on a Flexible NACA 0018 Finite Span Wing. In *AIAA Paper 2016-1554*, January 2016.

3. **E. Culler, J. Farnsworth**, C. Fagley, and T. McLaughlin. Driven versus "Free Flutter" Motion of a NACA 0018 Finite Span Rigid Wing. In *AIAA Paper 2017-4359*, June 2017.

Refereed Publications

1. **E. Culler**, C. Fagley, J. Seidel, T. McLaughlin, and **J. Farnsworth**. Developing a reduced order model from structural kinematic measurements of a flexible finite span wing in stall flutter. *J. Fluids and Structures*, **71**, pp. 56–69, April 2017.

2. **E. Culler**, C. Fagley, J. Seidel, T. McLaughlin, and **J. Farnsworth**. SPIV Flowfield Analysis Around Flexible Finite Span Wing Excited in Stall Flutter in the Wind Tunnel. In preparation for submission to *J. Fluids and Structures*, September 2017. (Forthcoming)

3. **E. Culler**, C. Fagley, J. Seidel, T. McLaughlin, and **J. Farnsworth**. Driven versus "Free Flutter" Motion of a NACA 0018 Finite Span Rigid Wing. In preparation for submission to *J. Fluids and Structures*, November 2017. (Forthcoming)

References

M. F. Barone and J. L. Payne. Methods for simulation-based analysis of fluid-structure interaction. Sandia Report SAND2005-6573, Sandia National Laboratories, 2005.

E. Culler, C. Fagley, J. Seidel, T. McLaughlin, and J. Farnsworth. Developing a reduced order model from structural kinematic measurements of a flexible finite span wing in stall flutter. *Journal of Fluids and Structures*, 71:56–69, Nov. 2017. doi: 10.1016/j.jfluidstructs.2017.03.010. URL http://dx.doi.org/10.1016/j.jfluidstructs.2017.03.010.

G. Dimitriadis and J. Li. Bifurcation behavior of airfoil undergoing stall flutter oscillations in low-speed wind tunnel. *AIAA Journal*, 47(11):2577–2596, November 2009. URL http://arc.aiaa.org/doi/abs/10.2514/1.39571.

E. H. Dowell and K. C. Hall. Modeling of fluid-structure interaction. *Annual Review of Fluid Mechanics*, 33:445–490, 2001.

L. E. Ericsson and J. P. Reding. Fluid mecahnics of dynamic stall part i. unsteady flow concepts. *Journal of Fluids and Structures*, 2(1):1–33, January 1988.

C. Fagley, J. Seidel, and T. McLaughlin. Experimental investigation of the aeroelastic behavior of a naca 0012 cyber-physical flexible wing. In *AIAA Paper 2015-2251*, Dallas, TX, June 2015. 33rd AIAA Applied Aerodynamics Conference, American Institute of Aeronautics and Astronautics. doi: 10.2514/6.2015-0250. URL http://dx.doi.org/10.2514/6.2015-0250.

C. Fagley, J. Seidel, and T. McLaughlin. Cyber-physical flexible wing for aeroelastic investigations of stall and classical flutter. *Journal of Fluids and Structures*, In Press:1–23, 2016.

Y. C. Fung. *An Introduction to the Theory of Aeroelasticity*. John Wiley, 1955.

H. J. Goett and W. K. Bullivant. Tests of n.a.c.a. 0009, 0012, and 0018 airfoils in the full-scale tunnel. Technical Report 647, National Advisory Committee for Aeronautics, 1938.

T. Hedrick. Software techniques for two- and three-dimensional kinematic measurements of biological and biomimetic systems. *Bioinspiration & Biomimetics*, 3(3):034001, 2008. doi: 10.1088/1748-3182/3/3/034001. URL http://dx.doi.org/10.1088/1748-3182/3/3/034001.

D. H. Hodges and G. A. Pierce. *Introduction to Structural Dynamics and Aeroelasticity*. Cambridge University Press, 2nd edition, January 2014.

J. C. Hunt, A. A. Wray, and P. Moin. Eddies, streams, and convergence zones in turbulent flows, 1988. URL https://ntrs.nasa.gov/search.jsp?R=19890015184.

J. Jeong and F. Hussain. On the identification of a vortex. *Journal of fluid mechanics*, 285:69–94, 1995. doi: 10.1017/S0022112095000462. URL https://doi.org/10.1017/S0022112095000462.

J. Larsen, S. Nielsena, and S. Krenk. Dynamic stall model for wind turbine airfoils. *Journal of Fluids and Structures*, (23):959982, 2007.

J. G. Leishman and T. S. Beddoes. A semi-empirical model for dynamic stall. *Journal of the American Helicopter Society*, 34(3):3–17, July 1989. doi: 10.4050/JAHS.34.3. URL http://dx.doi.org/10.4050/JAHS.34.3.

L. Librescu and P. Marzocca. Advances in the linear/nonlinear control of aeroelastic structural systems. *Acta Mechanica*, 178(3-4):147–186, 2005.

A. S. Mangalam, S. M. Mangalam, and P. M. Flick. Unsteady aerodynamic observable for gust load alleviation. In *AIAA Paper 2008-1725*, 2008.

W. J. McCroskey. The phenomenon of dynamic stall. Technical Memorandum NASA-TM-81264, National Aeronautics and Space Administration, NASA Ames Research Center; Moffett Field, CA, United States, March 1981. URL http://ntrs.nasa.gov/archive/nasa/casi.ntrs.nasa.gov/19810011501.pdf.

K. Onoue and K. S. Breuer. Vortex formation and shedding from a cyber-physical pitching plate. *Journal of Fluid Mechanics*, 793:229–247, 2016. doi: 10.1017/jfm.2016.134. URL https://doi.org/10.1017/jfm.2016.134.

N. A. Razak, T. Andrianne, and G. Dimitriadis. Flutter and stall flutter of a rectangular wing in a wind tunnel. *AIAA Journal*, 49(10):2258–2271, October 2011. doi: 10.2514/1.J051041. URL http://arc.aiaa.org/doi/abs/10.2514/1.J051041.

S. Sterbing-D'Angelo, M. Chadha, C. Chiu, B. Falk, W. Xian, J. Barcelo, J. M. Zook, and C. F. Moss. Bat wing sensors support flight control. *Proceedings of the National Academy of Sciences*, 108(27):11291–11296, 2011.

D. Tang and E. H. Dowell. Experimental and theoretical study on aeroelastic response of high-aspect-ratio wings. *AIAA Journal*, 39(8):1430–1441, August 2001. doi: 10.2514/2.1484. URL http://dx.doi.org/10.2514/2.1484.

D. Tang and E. H. Dowell. Limit-cycle hysteresis response for a high-aspect-ratio wing model. *Journal of Aircraft*, 39(5):885–888, September 2002. doi: 10.2514/2.3009. URL http://arc.aiaa.org/doi/abs/10.2514/2.3009.

Appendices

The following appendices represent the conference and journal publications resulting from this work that are currently available to the public on the publishers websites. They have not been attached to this report due to size limitations, but are available upon request from the PI as needed:

1. E. Culler, J. Farnsworth, C. Fagley, and T. McLaughlin. Spanwise Variation of Stall Flutter on a Flexible NACA 0018 Finite Span Wing. In *AIAA Paper 2016-1554*, January 2016.

2. E. Culler, C. Fagley, J. Seidel, T. McLaughlin, and J. Farnsworth. Developing a reduced order model from structural kinematic measurements of a flexible finite span wing in stall flutter. *J. Fluids and Structures*, **71**, pp. 56–69, April 2017.

3. E. Culler, J. Farnsworth, C. Fagley, and T. McLaughlin. Driven versus "Free Flutter" Motion of a NACA 0018 Finite Span Rigid Wing. In *AIAA Paper 2017-4359*, June 2017.

Symbols, Abbreviations, and Acronyms

List of Symbols

A	=	amplitude
AR	=	aspect ratio
b	=	wing span, m
c	=	wing chord, m
C_m	=	pitching moment coefficient
dW	=	differential work, $dW = -C_m d\alpha$
f	=	temporal frequency, Hz
J	=	rotational inertial, kgm^2/rad
k_θ	=	rotational stiffness, Nm/rad
M	=	mach number
q	=	dynamic pressure, pa
Q	=	balance between vorticity and rate of strain tensors, $Q = 1/2(|\Omega^2| - |S^2|)$
R_{XX}	=	normalized product of autocorrelation of variable X
S	=	wing area, m^2
t	=	time, s
T	=	period, s
$T_{x,y,z}$	=	translation (displacement) in the x,y, or z directions, m
U_∞	=	free-stream velocity, m/s
W_X, i	=	i^{th} mode weight of variable X
x	=	streamwise position, m
y	=	chord normal (vertical) position, m
z	=	spanwise position, m

Greek

α	=	angle of attack, ^{o}
γ	=	angular phase lag/lead, ^{o}
Γ_z	=	circulation aligned in the z direction, m^2/s
$\delta(X)$	=	error or uncertainty of variable X
$\Delta(X)$	=	increment in variable X
η	=	rotational damping, Nms/rad
θ	=	tip-twist angle or rigid body rotation angle, ^{o}
π	=	mathematical constant, 3.14159
ρ	=	air density, kg/m^3
τ	=	applied torque, Nm
ϕ	=	periodic phase angle, ^{o}
ω	=	angular frequency, rad
ω_θ	=	torsional natural frequency, Hz
ω_h	=	bending natural frequency, Hz
Ω_z	=	vorticity component in the z direction, $1/s$

Subscripts

Aero.	=	aerodynamically applied
Meas.	=	measured
Motor	=	motor applied
p	=	physical property
rms	=	root mean square
Struct.	=	structurally applied
Tip	=	wing tip condition
v	=	virtual property

List of Abbreviations

Hz	=	cycles per second
kg	=	kilogram
m	=	meter
N	=	newton
pa	=	pascal
rad	=	radian
s	=	second

List of Acronyms

DLT	=	Direct Linear Transformation
LCO	=	Limit Cycle Oscillation
NACA	=	National Advisory Committee on Aeronautics
PIV	=	Particle Image Velocimetry
SLA	=	Stereolithography
SPIV	=	Stereoscopic Particle Image Velocimetry
UCB	=	University of Colorado Boulder
USAFA	=	United States Air Force Academy